Physics – Uspekhi **60** (12) 1236 – 1267 (2017)

REVIEWS OF TOPICAL PROBLEMS PACS numbers: 61.43.Hv, **61.46. – w**, **72.15. – v**, **73.63. – b**

Metal nanostructures: from clusters to nanocatalysis and sensors

B M Smirnov

DOI: https://doi.org/10.3367/UFNe.2017.02.038073

Contents

Abstract. The properties of metal clusters and nanostructures composed of them are reviewed. Various existing methods for the generation of intense beams of metal clusters and their subsequent conversion into nanostructures are compared. Processes of the flow of a buffer gas with active molecules through a nanostructure are analyzed as a basis of using nanostructures for catalytic applications. The propagation of an electric signal through a nanostructure is studied by analogy with a macroscopic metal. An analysis is given of how a nanostructure changes its resistance as active molecules attach to its surface and are converted into negative ions. These negative ions induce the formation of positively charged vacancies inside the metal conductor and attract the vacancies to together change the resistance of the metal nanostructure. The physical basis is considered for using metal clusters and nanostructures composed of them to create new materials in the form of a porous metal film on the surface of an object. The fundamentals of nanocatalysis are reviewed. Semiconductor conductometric sensors consisting of bound nanoscale grains or fibers acting as a conductor are compared with metal sensors conducting via a percolation cluster, a fractal fiber, or a bunch of interwoven nanofibers formed in superfluid helium. It is shown that sensors on the basis of metal nanostructures are characterized by a higher sensitivity than semiconductor ones, but are not selective. Measurements using metal sensors involve two stages, one of which measures to high precision the attachment rate of active molecules to the sensor conductor, and in the other one the surface of metal nanostructures is cleaned from the attached molecules using a gas discharge plasma (in particular, capillary discharge) with a subsequent chromatography analysis for products of cleaning.

Keywords: metal clusters, metal nanostructures, laser ablation, percolation cluster, fractal fiber, bunch of nanowires, nanocatalysis, semiconductor conductometric sensor, metal conductometric sensor

B M Smirnov Joint Institute for High Temperatures,
Russian Academy of Sciences,
ul. Izhorskaya 13/19, 125412 Moscow, Russian Federation
E-mail: bmsmirnov@gmail.com

Received 17 November 2016, revised 11 February 2017
Uspekhi Fizicheskikh Nauk **187** (12) 1329 – 1364 (2017)
DOI: https://doi.org/10.3367/UFNr.2017.02.038073
Translated by B M Smirnov

1. Introduction

Investigations of clusters — systems of a restricted number of bound atoms — progress in a manner typical of any physical object. This manner consists of studying the nature and characteristics of the physical object in the first stage and studies based on this finding further ways to use separate physical properties of an object for application purposes. Subsequently, basic research on the object focuses on respective applications.

Studies of clusters as a physical object can be considered to have begun in the eighties, when the existence of magic numbers of atoms in a solid cluster was shown experimentally [1]. This led to particular interest in clusters and was the basis for detailed studies of clusters, which is also manifested in the development of experimental techniques and the creation of computer programs for numerical simulations of cluster properties. The results of these studies related to cluster properties and processes with their participation are reflected in a number of books devoted to clusters (for example, [2–4]).

In this review we consider metal clusters, focusing on the corresponding applications. First is the formation of metal

films on a dielectric surface as a result of attachment of a metal cluster beam to the surface. Such films are a nanometer-sized new material, a porous and amorphous metal. This material has specific properties which can be created depending on the parameters of the cluster beam. The resulting material, notably, can be used as a catalyst.

In this respect, so-called nanocatalysis generates the most interest, where a semiconductor substrate, usually of a metal oxide, is taken as the basis, and small supported metal clusters are bonded with the surface, forming a catalyst. The most frequently used system of this type contains gold clusters consisting of 10–20 atoms, which do not interact with each other. Attaching to the cluster, a reacting molecule causes a transition to an excited cluster configuration state, so that the chemical process takes place with the participation of bound molecules. When the chemical process is over, a cluster returns to the ground state configuration. In contrast to catalysis in chemistry, which may involve complex chemical compounds and may provide a change of the channel, nanocatalysis deals with simple systems and leads only to a change in the activation energy of the chemical process.

One peculiarity of clusters is that they only exist in the form of beams or inside a buffer gas, which prevents them from joining to form a macroscopic system. If the merging clusters are liquid, their joining leads to the formation of a compact system — a bulk metal. If these clusters are solid, as they join rare structures form, depending on the conditions under which the process of merging clusters occurs. Elements of such structures are nanometer-sized clusters, so that the structure is characterized by a large specific area of the surface. They can therefore be used as a filter or catalyst when a gas flow with reacting molecules propagates through a rare structure.

A promising application of metallic nanostructures is to use them as the basis for sensors in detecting active molecules in a buffer gas. We consider below only so-called conductometric sensors, where the concentration of active molecules in a buffer gas is measured by a change in the electric current through a conductor as a sensor basis due to the attachment of active molecules to the sensor surface. Since the action of active molecules on the conductor takes place only near its surface, i.e., at distances of the order of atomic sizes, the sensor wires are of nanometer sizes.

In the last two to three decades, progress has been made in the development of semiconductor sensors, which are characterized by a number of parameters, one of which is the sensitivity, i.e., the minimum measurable concentration of active molecules, and the selectivity, i.e., the possibility of determining the type of active molecules. Therefore, on the basis of the advantage of semiconductor sensors, it is necessary to take into account the fact that the metal sensor differs from the semiconductor one not only by the mechanisms of how they work, but also in the different ways they are used. Below, we look at the problems under consideration in more detail.

2. Some properties of metal clusters and nanostructures

2.1 Structures of metal clusters

Metal clusters, i.e., systems of a finite number of bound metal atoms, are characterized by a strong interaction between the metal atoms and a relatively large binding energy of atoms that leads to stable structures of atoms in the cluster, both for ground and excited configuration states. Transitions between the ground and excited configuration states determine the work of the cluster as a catalyst and are of interest from the standpoint of catalytic cluster properties. Therefore, we consider the atomic structures of metal clusters from this position.

Cluster magic numbers are a fundamental property of small clusters. The magic numbers of atoms in a cluster mean the highest cluster stability that is expressed in extremal values of some cluster parameters as a function of the number of cluster atoms, such as the binding energy of atoms in the cluster, the cluster ionization potential, and electron affinity. These parameters for clusters with magic numbers of atoms are higher compared to those in clusters which size is more or less by unity. Although the magic number of atoms in a cluster is shown up to a size corresponding to tens of thousands of atoms in a cluster, they are of interest only for small clusters. However, the main method of fixing the magic numbers of a cluster is to analyze mass spectrometry clusters formed in a buffer gas and extracted from it (for example, [1, 5–10]). Then, local maxima of cluster flows are observed at magic numbers of atoms in a cluster.

The first magic number of metal clusters, which refers to the most stable configuration of atoms in a cluster, is 13, which corresponds to the icosahedral structure of atoms [11]. In particular, in a gold cluster, this is observed in experiments [12–20]. The number 13 is the magic number for clusters with a short-range interaction of atoms [21], i.e., in the case of interaction between nearest neighbors only. Note that gold is a widespread material for a cluster, whose history begins in 1857 [22], when Faraday worked out a method to obtain gold particles of close sizes in colloidal solutions. This method was further modified by Zsigmondy [23] taking into account the fact that at a certain solution acidity the nanoparticle changes charge sign at a certain size. Then, nanoparticles attract metal ions in solution up to a certain size and grow, whereas nanoparticles of larger scales repel metal ions, i.e., the solution contains nanoparticles of almost the same size. This property was used to study the scattering of light by small particles [24], as well as in the study of growth of fractal aggregates [25–29]. Colloidal solutions containing gold nanoparticles of nearby sizes are used in various applications (for example, [30–33]).

It is convenient to demonstrate the competition of various structures of small clusters using the example of gold clusters, which can have the linear, zigzag, flat, and three-dimensional structures [34]. The last is typical for clusters containing tens of gold atoms and includes icosahedral, cellular, and tube-like structures [34–36]. A flat structure relates to the cluster ground state consisting of seven atoms, and it competes with the cluster structure of the ground state with the number of atoms of $n = 4-11$ [37]. An analysis of structures of charged gold clusters was made experimentally in [38] on the basis of the mobility measurement. Indeed, charged clusters of this size are selected by a mass spectrometer and are passed through a drift chamber with helium, where the clusters move under the action of a weak electric field.

Because of the small size of the helium atom compared to that of the gold atom and especially to its cluster, the cluster mobility of a given configuration may be calculated on the basis of the hard sphere model (for example, [39]) under the assumption that a cluster has a rigid boundary, i.e., the interaction potential between a helium atom and cluster

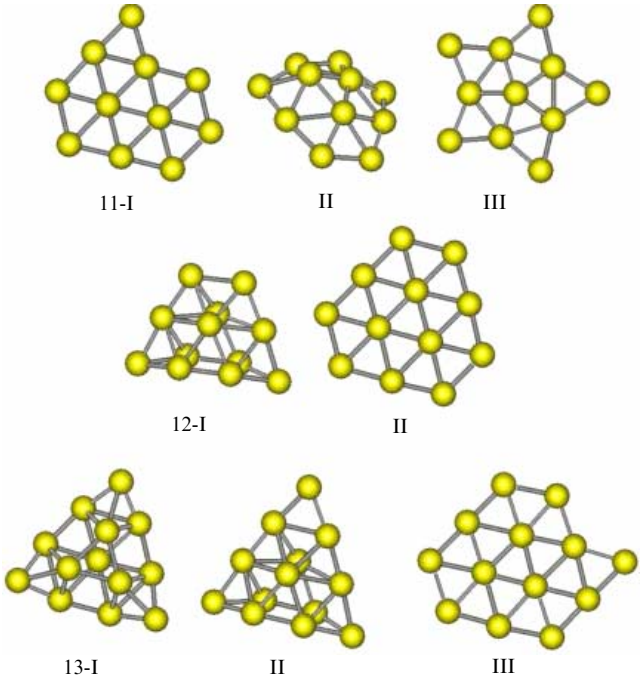

Figure 1. Configurations of the lower excited states of negatively charged gold clusters consisting of 11, 12, and 13 atoms [38]. Structures of more excited states are given on the right.

with the interaction energy of the order of the thermal energy changes sharply in a narrow range of distances between the colliding helium atom and the cluster for a given cluster configuration. This allows us to determine the mobility for a given cluster configuration of atoms. The mobilities for different cluster configurations differ by about 10%, whereas the accuracy of measurement of the mobility is about 1%. This allows cluster structures to be arranged in accordance with the excitation energies of a given configuration. In particular, the transition from flat to three-dimensional configurations of atoms in the cluster ground state for positively charged gold clusters Au_n^+ occurs at $n = 7$ [40], whereas for negative Au_n^- charged gold clusters this transition corresponds to $n = 12$ [41].

Figure 1 contains the energy sequence for the lower configuration states of negatively charged gold clusters consisting of 11, 12, and 13 atoms [38] obtained in this way, and Fig. 2 gives the possible configurations of planar and three-dimensional structures of atoms for gold clusters containing 10 atoms [34–36, 42].

Note that the energetic parameters of dielectric clusters with magic numbers of atoms, which correspond to filled atomic shells, differ significantly from the parameters of these clusters with other numbers of atoms. For metal clusters, such a strong dependence of the energetic parameters on the cluster number is absent. Moreover, along with the interaction between the atomic metal cores in clusters, the interaction between the valence electrons is essential. In particular, for clusters consisting of atoms with one valence electron, the coupling between electrons with different spin directions is of importance. This refers to alkali metals, as well as to so-called coin metals (copper, silver, gold) and leads to even-odd oscillations in energetic parameters of clusters. For example, such oscillations occur in the electron affinity of silver clusters [43, 44], and for clusters with an even number of atoms, the electron affinity is lower than that for clusters with an odd number of atoms.

2.2 Transition of an atomic system into a metallic state

In considering metal clusters and structures consisting of them, it is necessary to formulate their fundamental difference from other systems. The basic difference between metal systems and dielectrics is their high metal conductivity. This separation for macroscopic systems is readily apparent, because the conductivity of different materials varies from 10^9 up to 10^{-22} $\Omega^{-1}\text{cm}^{-1}$ [45–47], which encompasses 31 order of magnitude. But for clusters, parameters other than the material conductivity should be used to define the metal properties. Indeed, let us introduce the ionization cluster potential I, as well as the energy of the electron affinity of a cluster EA and, on the basis of these parameters, we introduce the correlation Mott–Hubbard energy U [48–52]

$$U = I - EA\,. \tag{2.1}$$

For metal clusters, correlation Mott–Hubbard energy U is zero. A valence electron of the metal cluster may then go freely outside the action of the cluster field, and electrons of large clusters can move freely over the cluster surface, which corresponds to a high conductivity of this object. For atoms and small clusters consisting of atoms, the relation $U = I - EA > 0$ holds true, i.e., ratio (2.1) is violated, so that atoms, molecules, and clusters of small sizes for each element are dielectric systems, but at certain sizes clusters may become metals. From the energetic standpoint, this corresponds to a small electron binding energy compared to the thermal energy. Below, we consider the transition to the metal cluster state using a simple example [53].

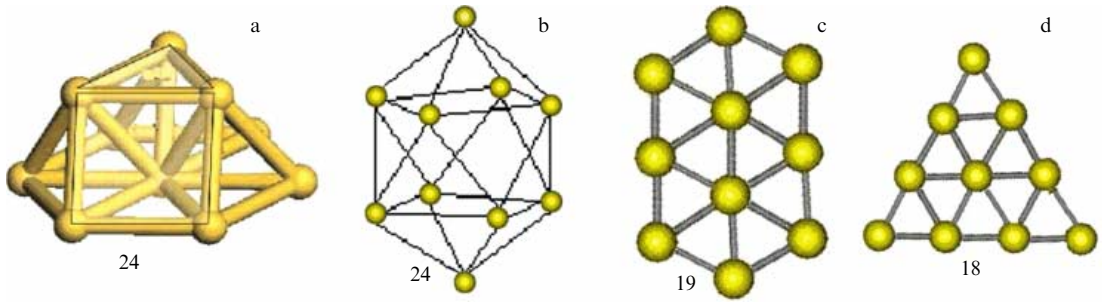

Figure 2. Configurations of atoms in a negatively charged gold cluster consisting of 10 atoms Au_{10} [34–36, 42]. (a) The basis of a cluster containing 7 atoms has a planar structure {111}; (b) the structure of a double cluster consisting of antiprisms; (c, d) atomic planar structures. The numbers indicate the number of bonds between nearest neighbors.

Indeed, atoms have a discrete spectrum, and as we move from atoms to clusters, the energy levels broaden and are transformed into energy bands. At a certain number of cluster atoms, the boundary is lost between the upper energy bands, and they are converted into a single energy band corresponding to the electronic excitation of the cluster. The cluster itself becomes a metallic system as soon as the band for the cluster ground state combines with the band corresponding to its lowest excited state. This occurs when the energies of the so-called HOMO (Highest Occupied Molecular Orbital) and LUMO (Lowest Unoccupied Molecular Orbital) states are joined, i.e, the excitation energy of the most weakly bound electron is zero. Note that in a system of a large number of atoms the HOMO energy is the excitation energy of the lowest excited state, and the LUMO energy corresponds to the energy of the atom electron affinity for this system. Since the interaction energy for excited states of a system is higher than that the ground state, the electron excitation spectrum becomes continuous, and this definition for transition to the metallic state [53] coincides with the Mott–Hubbard principle.

However, experimentally, it is convenient to use the Mott–Hubbard version, and we will demonstrate this for the case of mercury [54]. In accordance with the structure of the atom electron shell, small clusters are characterized by a filled electron s-band and a free p-excited band, and these bands are separated by a gap. The energy width of this gap, corresponding to the minimum energy of the s–p transition, decreases with increasing cluster size, and at some number of cluster atoms the s- and p-bands overlap, so that the cluster then becomes a metallic system in accordance with the Mott–Hubbard principle. In the experiment, the threshold energy of electron photodetachment from a negatively charged cluster Hg_n^- is compared with the threshold excitation energy of the cluster Hg_n (n is the number of cluster atoms). An approximation of these dependences as a function of the number of cluster atoms n to large clusters gives the number of cluster atoms, where the corresponding curves are intersected and the cluster becomes a metal system. In mercury, this intersection takes place at the following number of cluster atoms [54]:

$$n = 400 \pm 30\,. \tag{2.2}$$

This example, represented in Fig. 3, indicates the validity of the Mott–Hubbard principle, which relates to booth a macroscopic system and a cluster, and demonstrates the ability of experimental modeling of this transition to the metallic state.

Thus, the metallic property of a system of bound atoms is manifested in a high (metal) material conductivity, resulting in a low-energy excitation of valence electrons. This means that the lower excited states which are not occupied by electrons are separated from occupied electron states by a value below a thermal energy.

2.3 Metal nanostructures

The simplest fractal structure is a fractal aggregate, which is formed by joining of solid clusters. This is a loose structure, an example of which is shown in Fig. 4. Typically, the fractal aggregate is modeled as a system consisting of solid spherical particles of the same size, where nearest neighbors form a chemical bond in contact areas [55–59]. In other words, the nanostructure is constructed as a system of bound monomers.

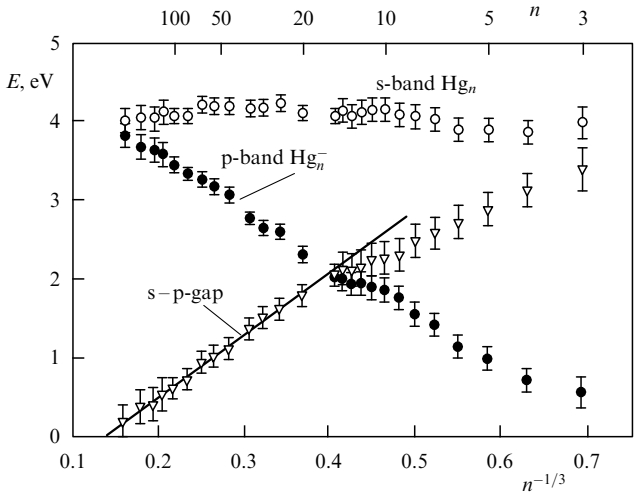

Figure 3. Threshold energy for photoabsorption of the neutral cluster Hg_n with a transition from the s-cluster band and that for a negatively charged cluster Hg_n^- with a transition from the p-cluster band [53], as well as the difference between these energies. The coincidence of these energies, i.e., the zero gap between the s- and p-bands, corresponds to a transition to the metallic state.

Fractal properties of the system [60, 61] characterize the correlation of the positions of monomers and are described by the fractal dimension D of the system, which is a parameter of its density. Namely, if we draw a sphere of radius R with a monomer in the center, the total mass M_a inside this sphere is

$$M_a = m_0 \left(\frac{R}{a}\right)^D , \tag{2.3}$$

where a is the monomer radius, m_0 is the monomer mass, and D is the fractal dimension of the aggregate. Note that for a compact aggregate which is completely occupied by particles — monomers — $D = 3$. (Since the standard designation of the fractal dimension D coincides with the notation of the diffusion coefficient, we denote the fractal dimension as α.) Then, the above formula (2.3) gives for the number n of elementary particles — monomers inside a fractal aggre-

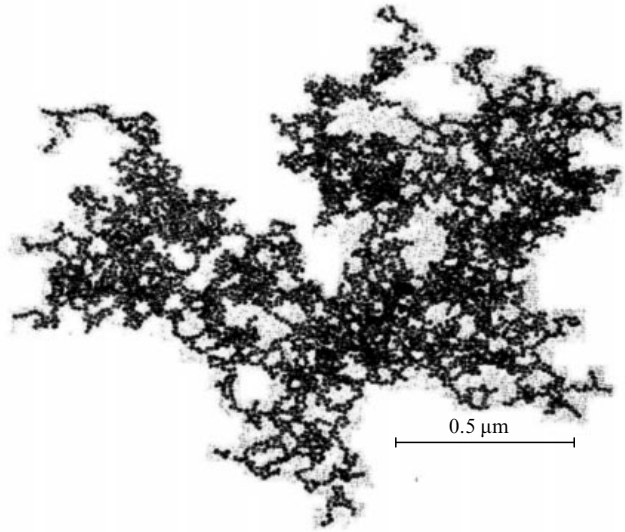

Figure 4. Fractal aggregate of silver [25].

gate —

$$n = \left(\frac{R}{a}\right)^{\alpha}, \tag{2.4}$$

where R is the average radius of the fractal aggregate.

The fractal dimension of an aggregate can be determined by a certain simulation of the growth process of a fractal aggregate. Note that, since the fractal aggregate is a chaotic system, the analysis of fractal aggregates constructed in the same scenario can lead to different fractal dimensions. We evaluate the accuracy of the aggregate fractal dimension based on the data used in [57, 62] and obtained by computer simulation of fractal aggregates in papers [63–68]. In the calculations used based on computer simulations of growth of fractal aggregates, the sticking probability of two small aggregates at their contact is taken as unity.

Let us give some results of statistical averaging based on calculations [63–68]. In the case of the kinetic regime of cluster growth, i.e., if joining clusters are moving along straightforward trajectories, the statistical value of the fractal dimension is $\alpha = 1.93 \pm 0.06$, and in the diffusive regime of cluster growth, i.e., in the case of Brownian motion of clusters, the fractal dimension is $\alpha = 1.77 \pm 0.03$. This is consistent with the fractal dimension $\alpha = 1.77 \pm 0.10$ for silver fractal aggregates formed in the solution and collected on a grate (Fig. 4). Note that in this case we have a diffusion limited aggregation (DLA) model [69], where growth of fractal aggregates is a result of joining smaller aggregates with the diffusion motion of clusters in a gas.

In turn, the number n of atoms in an individual cluster of radius a is connected with the Wigner–Seitz radius r_W by the relation [70, 71]

$$n = \left(\frac{a}{r_W}\right)^3. \tag{2.5}$$

For definiteness, we take the radius of an individual cluster to be $a = 5$ nm, and the fractal aggregate radius to be $R = 1$ μm, which corresponds to typical conditions. Table 1 contains values of parameters of the fractal structure for the metals under consideration. These parameters include the Wigner–Seitz radius [70, 71] for these metals, the metal atom mass m, the number n of cluster atoms according to formula (2.5), the density ρ of the metal at room temperature, and the mass of an individual cluster m_0 which follows from the formula

$$m_0 = \frac{4\pi a^3 \rho}{3}. \tag{2.6}$$

Table 1. Parameters of metallic fractal structures.

Parameter \ Metal	Cr	Fe	Ni	Cu	Pd	Ag	Pt	Au
r_W, nm	0.141	0.147	0.144	0.147	0.158	0.166	0.160	0.165
m, a.u.m.	52.0	55.8	58.7	63.6	106.4	107.9	195	197
ρ, g cm^{-3}	7.15	7.87	8.90	8.96	12.0	10.5	21.5	19.3
n	0.141	0.147	0.144	0.147	0.158	0.166	0.160	0.165
m_0, 10^{-18} g	3.8	3.6	4.1	4.1	5.6	4.9	9.9	9.1
M_a, 10^{-14} g	4.5	4.3	4.8	4.9	6.6	5.8	12	11
$\frac{dM}{\xi\, dS}$, μg cm^{-2}	4.8	5.2	5.9	6.0	8.0	7.0	14	13
ε, eV	3.79	3.83	4.13	3.40	3.67	2.87	5.4	3.65
$\frac{dE}{\xi\, dS}$, mJ cm^{-2}	34	35	40	31	27	18	38	23

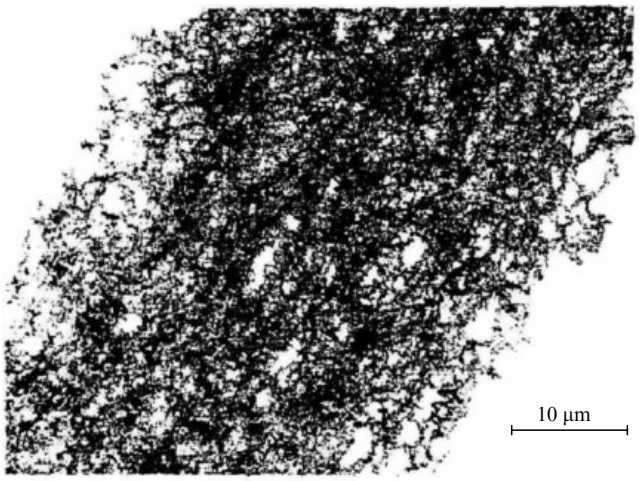

Figure 5. Fragment of a fractal fiber [74].

Table 1 also contains values of the mass of a fractal aggregate M_a in accordance with the formula $M_a = M_0 n$.

A fractal aggregate is a structure of micron size, and larger structures consist of fractal aggregates. Figure 5 shows a photograph of a fractal fiber. This nanostructure consists of fractal aggregates [72, 73] and is elongated in the direction of the electric field, which leads to the joining of fractal aggregates into fractal fibers as a result of the interaction of the induced dipole moments. Fractal fibers were first synthesized by Lushnikov et al. [74] by irradiation of a metal surface by a ruby laser (wavelength $\lambda = 693.4$ nm). A plasma torch arose in the region of irradiation of the metal surface with a laser beam where evaporation of metal atoms takes place. Next, fractal aggregates are formed as a result of a chain of processes [75], and the character of these processes has been studied in detail [56, 62–67, 69, 76, 77]. If the fractal aggregates exist in the buffer gas long enough, they can join in the aerogel as an isotropic fractal structure, or in other fractal structures [78, 57], because larger fractal aggregates become unstable with respect to the subsequent increase in size and, respectively, to reduce the density [78, 79]. In this case, the joining of fractal aggregates results from the interaction of dipole moments induced by an external electric field, which leads to the formation of elongated fractal structures — fractal fibers.

Let us note an important property of metals associated with their use as a catalyst [80–83]. This property applies to metals whose atoms contain noncompleted s- and d-electron shells [81] of macroscopic metals and their clusters. In the catalytic process, metals capture reactive molecules, and this process is accompanied by a transition between s- and d-electron bands of the metal [84]. When the chemical process takes place in the gas phase, it is convenient to use metal fractal fibers, which are thin metal objects with a developed inner surface, as a catalyst. In this process, the reacting molecules are located in a buffer gas flow. Analyzing the process of generation of fractal metal fibers for the catalytic process, we will consider further metals with unfilled s- and d-electron shells of their atoms. In addition, below we consider the character of propagation of a buffer gas flow through the fractal structure. Thus, the aim of this consideration is to analyze the processes of generation of fractal fibers and their interaction with buffer gas flows.

If a gas flow passes through a nanostructure, the scattering of gas molecules takes place on individual clusters which form the nanostructure. Therefore, it is convenient to model this nanostructure by a system of independent clusters which interact with the gas molecules. It is convenient to introduce the parameter of filling ξ, which characterizes the filling of a space by clusters of the fractal structure. Let us project the fractal structure onto the symmetry plane. If the fractal structure is located inside a tube, this plane is perpendicular to its axis. Let us define the filling parameter as

$$\xi = \pi a^2 N_{\rm cl} L\,, \tag{2.7}$$

where L is the layer thickness which is filled with a fractal structure, and $N_{\rm cl}$ is the number density of clusters of this structure. Since the projection of a single cluster onto a plane is equal to πa^2, then, when $\xi \ll 1$, the filling parameter is proportional to the total area occupied by the area of cluster projections of this structure. Next, let us place the fractal structure in a tube of radius R, and then the filling parameter ξ is the ratio of the sum of projection areas for clusters forming a fractal structure to the cross section area of the tube. Note that the filling parameter ξ characterizes the transparency of the fractal structure if the clusters are absorption balls of radius a. On the basis of the filling parameter ξ, we determine the mass M of the fractal structure per unit cross section area of the tube S, which is

$$\frac{{\rm d}M}{{\rm d}S} = m_0 N_{\rm cl} L = \frac{4a}{3}\,\rho\xi\,. \tag{2.8}$$

Let us determine the minimum energy E which is required to create the fractal structure of a metal, if the first step of this process is conversion of the metal into a gas of free metal atoms. Removal of each atom of the metal then requires consuming the atom binding energy of this metal ε, so that the minimum specific energy which is necessary to create a fractal structure is

$$\frac{{\rm d}E}{{\rm d}S} = \frac{\varepsilon}{m_0}\,\frac{{\rm d}M}{{\rm d}S} = \frac{4r_0\rho\varepsilon}{3m_0}\,\xi\,. \tag{2.9}$$

Table 1 contains the values of the specific mass of the fractal structure and the minimum specific energy of its formation for some metals.

2.4 Metal nanowires in superfluid helium

A specific fractal structure can be formed by introducing metal atoms in superfluid helium. This structure consists of metal nanowires, which are formed as a result of condensation and cluster growth for a vaporized metal in superfluid helium [85–87]. The superfluidity phenomenon is observed in helium with nuclei-isotopes ^{4}He and shows the ability to flow through narrow capillaries without viscous drag. Such a helium isotope, on the one hand, remains a liquid at low temperatures and, on the other hand, its atoms are bosons. Under these conditions, the superfluidity phenomenon is described in terms of the Landau two-liquid model [88], where liquid helium is divided into a normal liquid and a Bose condensate. Excitation of the liquid is determined by the formation of phonons and rotons, and the combination of these excitations produces the superfluidity of liquid helium at certain flow rates. This important phenomenon is described in detail in corresponding books [89–91].

One of the properties of superfluid helium, which is of interest for the processes under consideration, is the capture of impurity ions by liquid vortices [92, 93]. This property takes place for metal atoms inserted in superfluid helium. In considering the formation of metallic nanowires in superfluid helium, we use a simple model that, while not a theoretical substantiation of these processes, helps to explain them on the basis of reasonable considerations [94, 95]. The essence of this model is that superfluid helium repulses outside impurity atoms and particles. As a result, the vaporized metal atoms and further metal nanoclusters formed from them are locked inside some area, which is separated from the main volume of superfluid helium by a vortex, and this vortex keeps a metal in this region relatively long. In this case, the kinetics of conversion of a metal vapor in small nanoclusters is analogous to the process of nucleation of an atomic metal vapor in a buffer gas (for example, [96]). Namely, atoms join into small metal clusters-drops, and further, in turn, small clusters are joined in clusters of larger sizes until they become rigid.

The difference compared to the kinetics of growth of clusters in a buffer gas at some stages of nucleation may be connected with the high thermal conductivity of liquid helium, which leads to the formation of solid clusters at smaller cluster sizes. The principal difference in the kinetics of cluster growth takes place in the following stage, where solid clusters join in some structure in the region of their contact. As a result of solid clusters joining in a buffer gas, fractal aggregates are formed [72], i.e., a structure where neighboring clusters are in random directions with respect to a given direction. In superfluid helium, the clusters are arranged in one line forming a chain at the first stage of cluster growth.

Of course, the vortex length is restricted, and the observed length is estimated as $d \sim 100$ nm. Therefore, the vortex restricting a channel with metal clusters creates an anisotropy of a formed metal structure. In the case of clusters joined in a buffer gas, an isotropic fractal structure, fractal aggregates [72], is formed. At some vortex length in the course of structure growth in superfluid helium, the vortex comes off the metal surface, then the vortex with chain metal clusters inside it makes a diffusive motion in superfluid helium. If the vortex trajectory is intersected with that of another vortex containing a chain of metal clusters, these chains are joined in the contact region, and subsequent growth leads to the formation of fractal structures, elements of which are nanowires of a length of the order of 100 nm and a radius of a few nanometers. This structure may be attached to walls or to other elements of a motionless construction, so that after helium removal this structure exists stably inside a buffer gas.

As an example, Fig. 6 represents a metallic nanostructure which is located on a surface. The metal structures under consideration may be used as a catalyst [97–99], as can other nanostructures. In terms of this review, these nanostructures are of interest as the basis of sensors.

3. Generation of intense beams of metallic clusters

3.1 Interaction of laser pulse with a metal surface

Generators of clusters have existed for more than half a century (see [101–103]). During this time, various methods and schemes of cluster generation have been developed (see, for example, [104]). We consider below some of these methods which allow generating intense beams of clusters. Only in the

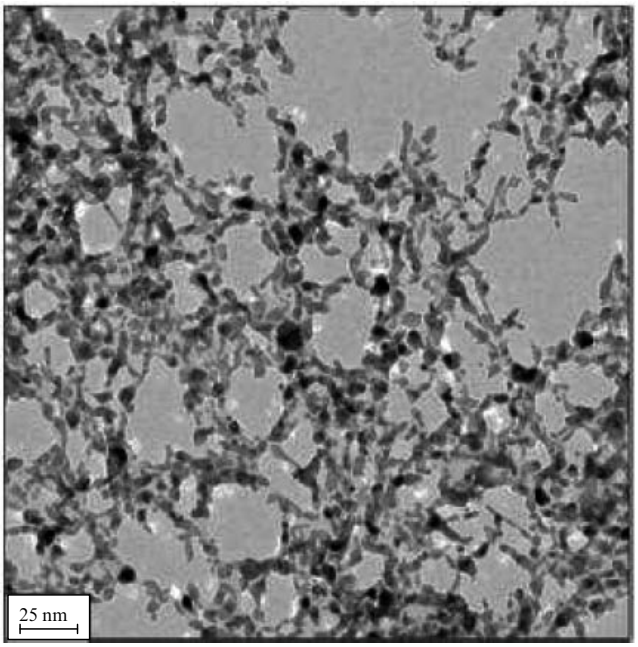

Figure 6. Structure obtained by laser ablation of the alloy Au–Cu in liquid helium and set down on a grid covered with carbon after annealing at 723 K [100].

case of intense cluster beams are solid cluster structures formed, which can be used as a filter, a catalyst, or a sensor conductor. Note that the first stage of the process of generation of metal clusters in all cases is the formation of a metal atomic vapor, and it is subsequently converted into a gas of clusters as a result of atom joining and atom attachment to the clusters. At the stage of cluster solidification and under corresponding conditions, their association leads to the formation of nanostructures, i.e., fractal aggregates, aerogels, and fractal fibers [105, 106].

The simplest way to generate metal vapor from macroscopic metal consists of irradiating the metal surface with a powerful laser that causes its evaporation. As a result, a beam of evaporated metal atoms is formed in the irradiated region of the surface. In the case of a continuous laser beam, a metal plasma is formed due to the interaction of evaporated metal atoms with the laser beam and absorbs radiation at a certain stage of the process. In this case, the laser beam energy is transmitted to the plasma, and finally electric breakdown occurs in the plasma [107]. Hence, a pulse laser source is used to create the metal vapor. In a similar way, the creation of the metal vapor may be a result of irradiating the surface with a plasma beam.

Let us consider the process of absorption of an electromagnetic wave by a metal surface, which is accompanied by heating of the target. The character of the process of electromagnetic wave absorption with a metal target is analyzed in book [108], and the results of this analysis will be used. The interaction of the electromagnetic wave with the metal surface is characterized by the metal surface impedance ζ, which is introduced as [108]

$$\zeta = \sqrt{\frac{\omega}{8\pi\Sigma}}, \tag{3.1}$$

where ω is the frequency of the electromagnetic wave, and Σ is the metal conductivity at a given temperature. This parameter characterizes the nature of interaction of an electromagnetic wave with the metal surface which follows from interaction of metal valence electrons with the electromagnetic wave. Subsequently, the energy which is received by electrons from the wave is transferred from the valence electrons to atomic cores through the same mechanism that determines the metal conductivity.

Let us approximate the temperature dependence of the metal conductivity as

$$\Sigma(T) = \Sigma_0 \left(\frac{T}{T_0}\right)^k, \tag{3.2}$$

where T is the metal temperature, $T_0 = 300$ K, and parameters of this formula (3.2) obtained from the data in [109] are given in Table 2. For simplicity, we take an incident electromagnetic wave to be perpendicular to the metal surface. In this case, the probability of absorption of the electromagnetic wave by the metal surface at normal incidence is given by [108]

$$P_{\text{abs}} = 1 - R = 4\zeta\,, \quad \zeta \ll 1\,, \tag{3.3}$$

where R is the probability of reflection of the electromagnetic wave from the surface. Metals with a high conductivity are

Table 2. Thermal and energy parameters of metals in the course of evaporation of the metal surface with the formation of free metal atoms.

Parameter \ Metal	Cr	Fe	Ni	Cu	Pd	Ag	Pt
T_{m}, K	2180	1812	1728	1358	1828	1235	2041
T_{b}, K	2944	3023	3100	2835	3236	2435	4098
N_{sat} ($T = 2000$ K), 10^{14} cm^{-3}	3.2	2.0	0.74	11	1.1	190	4.0×10^{-4}
D_{m} ($T = 2000$ K, $p = 1$ atm), cm^2 s^{-1}	41	38	37	35	28	28	26
ρ_{m}, g cm^{-3}	6.3	6.98	7.81	8.02	10.38	9.32	19.77
c_{p}, J g^{-1} K^{-1}	0.450	0.449	0.445	0.384	0.244	0.235	0.133
κ ($T = 300$ K), W cm^{-1} K^{-1}	0.937	0.802	0.907	4.01	0.718	4.29	0.716
κ ($T = 1200$ K), W cm^{-1} K^{-1}	0.654	0.283	0.762	3.39	—	3.61	0.826
n	0.26	0.75	0.13	0.12	—	0.12	0.10
χ ($T = 300$ K), cm^2 s^{-1}	0.33	0.26	0.26	1.3	0.28	2.0	0.27
Q ($T = 2000$ K), kJ cm^{-3}	5.7	6.3	7.0	6.2	5.1	4.4	5.3
Σ, 10^{16} s^{-1}	7.1	9.0	12	52	8.3	55	8.3
k	1.04	1.78	1.53	1.14	0.91	1.13	0.99
ζ ($T = 2500$ K)	0.16	0.14	0.13	0.08	0.15	0.08	0.15
T_{tr}, 10^3 K, $p = 1$ atm	2.95	3.2	3.45	2.8	3.2	2.358	4.1

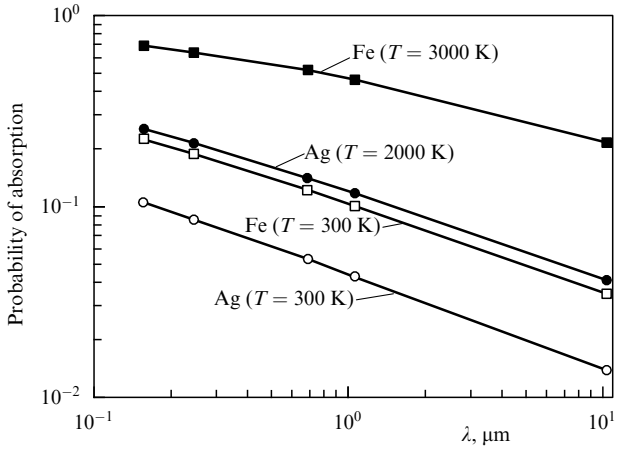

Figure 7. Probability of absorption of an electromagnetic wave directed perpendicularly to the plane of a metal surface at indicated temperatures. Icons correspond to the wavelength of an excimer laser F_2 (λ = 157 nm), excimer KrF-laser (λ = 248 nm), ruby laser (λ = 694 nm), neodymium laser (λ = 1.064 μm), and CO_2 laser (λ = 10.6 μm).

characterized by a small parameter (3.1), i.e., $\zeta \ll 1$, and the probability of reflection of an electromagnetic wave is close to unity; in violation of this criterion, the probability of absorption of an electromagnetic wave is equal to one. It is therefore convenient to approximate the probability of absorption of an electromagnetic wave by the following expression:

$$P_{\rm abs} = \frac{4\zeta}{1+4\zeta}\,, \tag{3.4}$$

because $P_{\rm abs} \leqslant 1$. Figure 7 contains the dependence of the absorption probability $P_{\rm abs}$ of an electromagnetic wave with the metal surface on the wavelength. As is seen, the absorption probability of an electromagnetic wave is small at room temperature. However, there is a threshold value for absorption of an electromagnetic wave [parameter (3.1)], and the absorption process leads to an increase in the surface temperatures, which causes an increasing probability of absorption. As an example, Fig. 7 gives the dependence of the absorption probability of an electromagnetic wave with bulk silver and iron at different temperatures.

Let us introduce the penetration depth $\delta_{\rm p}$ of an electromagnetic wave inside the metal as [108]

$$\delta_{\rm p} = \frac{\lambda\zeta}{4\pi}\,. \tag{3.5}$$

Note that for electromagnetic radiation generated by a laser in the visible and infrared spectral ranges we have $\zeta < 1$. From this, it follows that the penetration depth is less than the length of the electromagnetic wave, which leads to a small depth of the region in the vicinity of the metal surface where the electromagnetic wave interacts with the metal. Table 3 contains the value of the parameter ζ (3.1), and the depth of penetration of the electromagnetic wave (3.5) into the metal.

Absorption of an electromagnetic wave by the metal surface leads to its heating, causing the evaporation of the metal surface. For a metal surface with a high conductivity, the thermal equilibrium in an absorbed layer is established as a result of collisions of valence electrons with the ionic lattice during short times of the order of 10^{-14} s. One can characterize the surface layer which is responsible for absorption of an

Table. 3. Parameters of a beam of metallic atoms formed on a metal surface that is heated to a temperature of 5000 K at a laser pulse duration of 10^{-9} s.

Parameter \ Metal	Cr	Fe	Ni	Cu	Pd	Ag	Pt	Au
ζ	0.14	0.34	0.21	0.06	0.10	0.10	0.12	0.065
$\delta_{\rm p}$, nm	12	29	18	4.9	8.9	8.9	10	5.5
$P_{\rm abs}$	0.35	0.58	0.46	0.19	0.30	0.30	0.32	0.21
$p_{\rm sat}$, atm	450	150	76	560	120	1900	14	250
$N_{\rm sat}$, 10^{19} cm^{-3}	17	12	13	15	15	41	2.1	37
$N_{\rm m}$, 10^{22} cm^{-3}	7.3	7.6	8.0	7.6	5.9	5.2	6.1	5.3
$N_{\rm sat}/N_{\rm m}$, 10^{-3}	2.3	1.6	1.6	2.0	2.6	7.9	0.3	7
$J_{\rm ev}$, 10^7 W cm^{-2}	1.4	1.0	1.1	1.0	0.9	1.9	0.034	0.004
$J_{\rm th}$, 10^8 W cm^{-2}	3.4	3.4	4.2	7.2	2.8	6.5	2.9	5.6
$J_{\rm ev}/J_{\rm th}$	0.04	0.03	0.03	0.014	0.03	0.03	0.001	0.0008

electromagnetic wave by a temperature T. Let us connect the flux of evaporated atoms from the surface with this temperature, assuming the evaporated atoms leave to a dense buffer gas, which borders the metal. Because of thermal equilibrium, the number density of metal atoms near the surface coincides with the saturated vapor number density $N_{\rm sat}(T)$, which is estimated as

$$N_{\rm sat}(T) \sim \exp\left(-\frac{\varepsilon}{T}\right). \tag{3.6}$$

Table 1 gives the binding energies of metal atoms ε, and Table 2 contains the values of the metal melting temperature $T_{\rm m}$ and the boiling point $T_{\rm b}$ of these metals. In addition, Table 2 shows the values of the number density of atoms $N_{\rm sat}$ at the saturated vapor pressure at T = 2000 K.

Under these conditions, we have the following expression for the energy flux $J_{\rm ev}$ due to atom evaporation if the atoms move away from the surface:

$$J_{\rm ev} = \varepsilon D_{\rm m}\frac{\partial N_{\rm m}}{\partial z}\,, \tag{3.7}$$

where $D_{\rm m}$ is the diffusion coefficient of metal atoms in a buffer gas (argon), and $N_{\rm m}(z)$ is the number density of metal atoms at a distance z from the metal surface. Table 2 contains the values of the diffusion coefficient $D_{\rm m}$ for metal atoms in argon at a pressure of 1 atm and temperature T = 2000 K. Below, we take $\partial N_{\rm m}/\partial z \approx N_{\rm sat}/l$, where $l \approx 1$ mm is the minimum size of the vortices formed near the hot metal surface. This value can be estimated on the basis of the theory of convective instability of a liquid or gas [110]. Accordingly, the energy flux $J_{\rm ev}$ consumed on evaporation of metal atoms is given by

$$J_{\rm ev} = \frac{\varepsilon D_{\rm m} N_{\rm sat}(T)}{l}\,, \tag{3.8}$$

and its temperature dependence for some metals is represented in Fig. 8a.

We first consider the regime of absorption of an electromagnetic wave by a metal with a relatively long pulse, being guided by the pulse duration τ = 1 μs. In this regime, the basic energy loss from a metal surface heated from absorption of an electromagnetic wave results from heat transport inside the metal due to thermal conductivity; values of the thermal conductivity of metals are given in Table 2. These values are taken from [109] and refer to the temperatures T = 300 K and T = 1200 K. The temperature dependence for the thermal conductivity of metals $\kappa(T)$

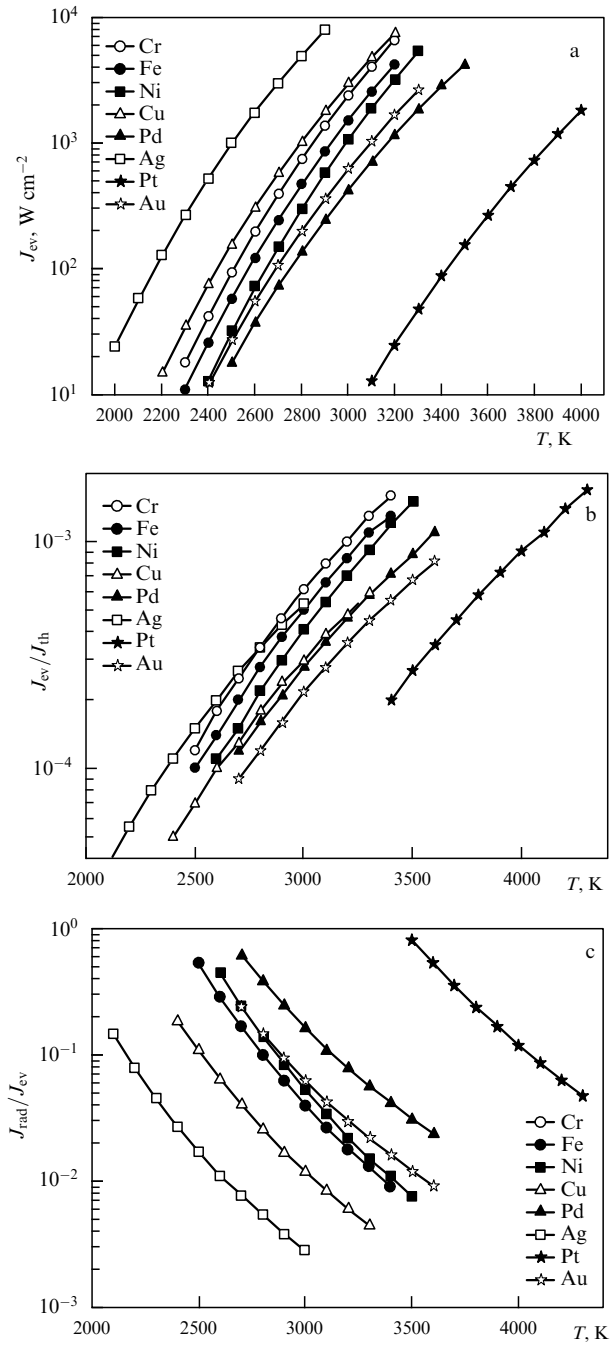

Figure 8. Interaction of laser radiation flux with a metal surface. (a) The energy flux consumed on atom evaporation from the metal surface (J_{ev}) at the temperature T. (b) The efficiency of atom evaporation from the metal surface as the ratio of energy flux due to evaporation (J_{ev}) and heat transport (J_{th}) as a result of the thermal conductivity in a bulk metal. (c) The ratio of the radiative energy flux J_{rad} to the evaporation energy flux J_{ev} from the metal surface.

may be represented in the form

$$\kappa(T) = \kappa_0 \left(\frac{300}{T} \right)^n . \tag{3.9}$$

Values for n obtained on the basis of data in [109] are given in Table 2.

Let us construct the thermal diffusivity coefficient χ as

$$\chi(T) = \frac{\kappa(T)}{c_p \rho} , \tag{3.10}$$

where c_p is the metal heat capacity at constant pressure, and ρ is the metal density.

Values of the thermal diffusivity coefficient for metals χ, obtained on the basis of formula (3.10), are given in Table 2 and are used for evaluations. The mean square distance $\overline{(\Delta x)^2}$ of heat propagation during time t in the direction perpendicular to the surface is given by

$$\overline{(\Delta x)^2} = 2\chi(T)\, t . \tag{3.11}$$

Note that in this case the heat is distributed only perpendicularly to the surface, since the radius of the irradiated area ρ_0 greatly exceeds the distance over which heat propagates in the transverse direction. We have for the energy flux J_{th}, which is consumed upon metal heating,

$$J_{th} = \frac{Q\Delta x}{\tau} = \frac{Q\sqrt{2\chi(T)}}{\sqrt{\tau}} , \tag{3.12}$$

where τ is the pulse duration. Let us introduce the energy density Q per unit volume required for heating the metal target by temperature ΔT under the above conditions, if the final metal temperature is much higher than room temperature $\Delta T \approx T$. We have

$$Q = c_p \rho \Delta T . \tag{3.13}$$

Table 2 contains values of this parameter at metal heating up to the temperature $\Delta T = 2000$ K. Since the parameters used relate to room temperature, the results of Table 2 are considered estimations.

Let us define the efficiency of the evaporation process from the metal surface as the ratio of the energy flux J_{ev} required for atom evaporation to the energy flux J_{th} consumed upon metal heating, i.e.,

$$\delta = \frac{J_{ev}}{J_{th}} = \frac{J_{ev}\sqrt{2\chi(T)}}{Q\sqrt{\tau}} . \tag{3.14}$$

Figure 8b gives the temperature dependence of the efficiency of atom evaporation J_{ev}/J_{th} from the metal surface at a pulse duration $\tau = 1$ μs. As is seen, the efficiency is low for the formation of metal clusters and, subsequently, metal nanostructures by heating the metal surface. However, since the mass of a metal nanostructure is small, the regime under consideration involving the use of laser and plasma sources of a middle power may be used to produce fractal metallic nanostructures.

Since the metal surface is strongly heated as a result of the absorption of an electromagnetic wave, radiation from the metal surface may make a contribution to its energy balance. Let us compare the energy flux J_{ev} for atom evaporation with the energy flux J_{rad} due to radiation from this surface, which is given by the formula

$$J_{rad} = a(T)\, 4\pi r^2 \sigma T^4 , \tag{3.15}$$

where σ is the Stephan–Boltzmann constant, and $a(T)$ is the grey coefficient of the metal surface averaged over frequencies. In accordance with the definition, the grey coefficient $a(\omega, T)$ of the metal surface for a given frequency ω is given by [108]

$$a(\omega) = \zeta \left[2\ln\left(\frac{1}{\zeta}\right) - \ln 2 - \frac{\pi}{2} + 1 \right] , \quad \zeta = \sqrt{\frac{\omega}{8\pi\Sigma}} < 1 . \tag{3.16}$$

Taking into account the weak frequency dependence of the grey coefficient, we use the Wien law [111], according to which the wavelength λ of blackbody radiation for the maximum radiative flux is connected with the radiative temperature T by the relation $\lambda = 0.29/T$, where the radiative temperature is expressed in K and wavelength in centimeters. This allows us to replace frequency with the radiative temperature in formula (3.16) in accordance with the Wien law. Table 2 contains values of the grey coefficient for metals, and these data confirm the smallness of the parameter $\alpha = \zeta^2$ in formula (3.16). Figure 8c also gives the ratio of the energy fluxes $J_{\text{rad}}/J_{\text{ev}}$, which are determined by formulas (3.8) and (3.15). This implies that radiation from the hot metal surface makes a small contribution to the energy balance of the surface compared to the evaporation flux.

Thus, the analysis fulfilled exhibits a low efficiency of atom evaporation from the metal surface by the action of a laser beam in this regime with pulse durations of the order of 1 μs. This process has a threshold, because it is necessary to heat the surface region to a certain temperature in order to realize this process. A basic loss of the absorbed power in the metal results from its heating, so that the shorter the laser pulse the higher the evaporation efficiency. Note that the metal surface temperature increases with time at a constant flux density of the laser beam, because the heat flux due to thermal conductivity decreases at large distances with time. Above, we assume the surface temperature in the course of its irradiation with the laser beam to be independent of time. The above regime of interaction of laser radiation with a metal surface refers to the laser radiative fluxes $J \sim (10^6 - 10^7)$ W cm^{-2} and the pulse duration $\tau \sim 1$ μs. This regime corresponds to that of [74], where fractal fibers were obtained, as well as in [112, 113], where metal fractal structures such as an aerogel were formed from vaporized material.

Let us consider another regime of interaction of a laser beam with a metal surface for a high-intensity laser beam and smaller pulse time. Here, the power of the absorbed laser radiation is compensated by the power consumed to evaporate metal atoms and form the atomic beam [114, 115]. The character of atomic beam formation for a sharply heated surface with a laser beam is described in [107, 116–118]. By analogy with the above regime, the first step of this process is the formation of free metal atoms on the metal surface. However, the density of evaporated atoms is small in the above regime, and each of these atoms penetrates in a buffer gas independently of the other ones and propagates in it as a result of diffusion. In this regime, the evaporated vapor pressure $p_{\text{sat}}(T)$ is high compared to the buffer gas pressure p in accordance with the criterion

$$p \ll p_{\text{sat}} . \tag{3.17}$$

In the second regime, evaporated metal atoms form a beam that 'breaks through' the buffer gas and penetrates deep into it. In accordance with the character of this process [107, 116–118], a metal vapor creates the pressure $p_{\text{sat}}(T)$ on a metal surface and is characterized near the surface by a semi-Maxwell distribution function over atom velocities with the metal surface temperature T. In other words, the distribution function at atomic velocities near the surface is the part of the Maxwell distribution function where atoms are removed from the surface. Upon removal from the surface at distances of a few mean free paths, atom movement is converted into a beam. Then, the Maxwell distribution function at atomic velocities is realized with beam temperature T_{b}, and the beam propagates with velocity c_{s}. These beam parameters may be connected with initial parameters of an evaporated vapor that follows from the conservation laws for density and energy fluxes on the metal surface and the beam near the surface. We have an average energy of metal atoms on the surface and the beam

$$\frac{3}{2}\, T = \frac{1}{2}\, mc_{\text{s}}^2 + \frac{3}{2}\, T_{\text{b}} . \tag{3.18}$$

Here, m is the atom mass, the speed of the sound is $c_{\text{s}} = (\gamma T/m)^{1/2} = 5T/3m$ in the atomic beam, and the parameter γ for an atomic gas, that is, the ratio of the capacities at constant pressure and volume, equals 5/3. From this, the relation

$$T_{\text{b}} = \frac{9}{14}\, T = 0.64T . \tag{3.19}$$

follows between the atom temperatures in the beam of metal atoms and near the metal surface.

The flux of metal atoms is conserved both on the metal surface and in the beam of metal atoms, where it is equal to $c_{\text{s}} N_{\text{b}}$. Since the average velocity of atoms for the semi-Maxwell velocity distribution near the surface is $(2T/(\pi m)^{1/2}$, we have from the equality of atom fluxes near and far from the surface

$$N_{\text{b}} = \sqrt{\frac{6T}{5\pi T_{\text{b}}}}\, N = \sqrt{\frac{28}{15\pi}}\, N = 0.77N , \tag{3.20}$$

where N is the number density of atoms on the metal surface, and N_{b} is the number density of metal atoms in the beam not far from the surface.

In both the above regimes, the laser beam energy is consumed mostly on heating the metal sample, and heat propagates inside the target due to the metal thermal conductivity. Note that for the metals under consideration the transition to the beam mechanism increases the atom flux from the metal surface by about two orders of magnitude. In accordance with formula (3.12), an increase in the pulse duration leads to a decrease in the energy flux due to the metal thermal conductivity. Therefore long pulses seem to be more proper. However, because the pulse energy is restricted, at its given value short pulses are more profitable, since they heat the metal surface more strongly, which leads to an increasing flux of evaporated atoms. Notably, Table 3 contains parameters of the interaction of the laser pulse with the metal surface, where the laser beam generated by a neodymium laser with a wavelength of 1.06 μm and pulse duration of 1 ns leads to surface heating to a temperature 5000 K. Since the metal parameters at this temperature are obtained by approximation of data at low temperatures, these data should be considered as estimates. Nevertheless, these results give a representation of the character of formation of the evaporated atom beam and its parameters.

We are guided by the metal surface temperature $T = 5000$ K that is reached under the action of the laser beam. At this temperature and typical laboratory pressures of a buffer gas, the saturated vapor pressure on the metal surface p_{sat} satisfies criterion (3.17), i.e., in this case, the second regime of atom evaporation from the metal surface is realized, when the atomic beam is formed near the surface. Under these conditions, a remarkable part of the laser pulse energy is absorbed and is consumed for heating the metal

target. The depth of penetration of an electromagnetic wave into the metal is of the order of 10 nm, which is significantly smaller than the wavelength of an electromagnetic wave. In addition, a small portion of the surface layer of a molten metal is converted into vapor, $N_{\rm sat}/N_{\rm m}$ ($N_{\rm sat}$ is the number density of metal atoms at the saturated vapor pressure, $N_{\rm m}$ is the number density of metal atoms in the surface layer), i.e., most of the metal atoms remain in the surface layer in the bound state. Next, the efficiency of formation of free metal atoms is of the order of one percent at the surface temperature 5000 K, except gold and platinum surfaces.

5w > The beam regime of evaporation of metal atoms from the surface holds true for short and intense pulses of laser radiation. Let us estimate the minimum pulse duration τ during which a thermal wave of heat transfer due to thermal conductivity is not formed. According to formula (3.11), we have

$$\tau \sim \frac{\delta_{\rm p}^2}{\chi}\,. \tag{3.21}$$

Since $\delta_{\rm p} \sim 10$ nm, $\chi \sim 1$ cm^2 s^{-1}, we have for the minimum pulse duration $\tau \sim 1$ ps. If the surface temperature is 5000 K, the characteristic value of the energy flux is of the order of 0.1 J cm^{-2}.

Table 4 contains values of the temperature $T_{\rm tr}$, at which the transition proceeds between two regimes of metal atom evaporation from the surface at a buffer gas pressure of 1 atm, i.e., $p_{\rm sat}(T_{\rm tr}) = 1$ atm. Depending on the degree of heating, both evaporation regimes are possible. As is seen, the higher efficiency of metal atom formation as a result of evaporation from the metal surface under the laser pulse action is realized in the beam regime. In the first stage of this regime, a dense vapor is formed near the surface and is subsequently converted into a beam of metal atoms. Most of the surface atoms remain bonded, which corresponds to the criterion

$$N_{\rm m} \gg N_{\rm sat}(T)\,, \tag{3.22}$$

where $N_{\rm m}$ is the number density of surface atoms, and $N_{\rm sat}(T)$ is the number density of atoms in the metal saturated vapor at temperature T. In this case, near the surface an equilibrium is established between bound and free atoms, and then a beam of free metal atoms is formed. Hence, the beam regime of formation of metal atoms is realized at temperatures

$$T \ll T_{\rm max}\,, \tag{3.23}$$

in accordance with criterion (3.22), and at $T_{\rm max}$ surface atoms form a dense gas, i.e, $N_{\rm sat}(T_{\rm max}) = N_{\rm m}$. Table 4 contains values of the parameter $T_{\rm max}$ for some metals. As is seen, there is a wide range of temperatures at which the beam mechanism is realized for evaporation of surface metal atoms under the action of the laser pulse. Note that the pulse duration for both regimes of atom evaporation is small, $\tau < 1$ μs [107], so that laser breakdown of an evaporated vapor has no time to occur.

Table. 4. Transition temperatures for the beam regime of evaporation of metal atoms from a metal surface under the action of a laser pulse.

Parameter \ Metal	Cr	Fe	Ni	Cu	Pd	Ag	Pt	Au
$T_{\rm tr}$, 10^3 K, $p=1$ atm	2.95	3.2	3.45	2.8	3.2	2.358	4.1	3.0
$T_{\rm max}$, 10^4 K	1.6	1.8	1.5	2.4	1.7	1.8	2.1	1.8

Thus, it is convenient to use laser pulses with a duration of ~ 1 ns to generate metal atoms from the metal surface and a radiative flux of $10^8 - 10^9$ W cm^{-2}. In this case, the efficiency of using the laser energy for atom vaporization can reach a few percent. It should be noted that contemporary producers make lasers with suitable parameters. In particular, the neodymium laser STA-01-8 of the wavelength 1.06 μm made by the Standa company (Lithuania) [119] is characterized by a pulse duration of 0.5 ns, pulse energy of 0.2 mJ, and pulse repetition rate of 1 kHz.

In particular, such a laser was used in [97–99], where nanometer metal filaments were generated in superfluid helium, and the specific energy of a weakly focused pulse was 1 J cm^{-2}. According to the data in Table 3, the metal surface is heated to a temperature of approximately 6000 K. A typical distance of propagation of a thermal signal for this time is about 0.2 μm, according to formula (3.11). The penetration depth of a laser pulse depends on the metal type and, according to formula (3.5), is of the same order of magnitude. This demonstrates the high efficiency of the vaporization process by irradiating a target with a neodymium laser.

The signal of a neodymium laser can be significantly shortened. For example, a laser from the Passat firm (Canada) [120] allows one to receive pulses 8 ps in duration, 0.55 mJ in energy, and with a repetition rate of 400 Hz. Weak focusing of this signal provides the specific power for the beam regime of the evaporation process from the metal surface.

Summing up the above analysis, we note different regimes for generating metal atoms as a result of irradiation of the metal surface. The pulse duration is greater than a picosecond, during which an equilibrium is established between the electromagnetic wave and electrons of the metal surface, so that the electron temperature is determined by the radiation power. If the temperature of surface electrons is less than $T_{\rm tr}$ (Table 4), the number density of free metal atoms near the surface is lower than the number density of buffer gas atoms. In this regime of evaporation, metal atoms are removed from the metal surface as a result of diffusion in the buffer gas. At radiation powers at which the surface temperature exceeds $T_{\rm tr}$, metal atoms are removed from the metal surface in the form of a beam. In addition, at high surface temperatures, a beam of evaporated metal atoms contains electrons and ions, and the radiative flux directed to the metal surface may not reach the metal surface and be absorbed in the beam.

3.2 Generation of metal clusters from a magnetron discharge

The most widely used method of generating metal clusters is based on magnetron discharge. Initially, in [121] magnetron discharge represented practically a glow discharge, where a magnetic field was applied along the electric field, and if the magnetic field was large enough, the electrons became magnetized, changing the discharge parameters compared with the glow ones. Subsequently, this scheme has been modified [122–125] through the use an appropriate magnetic field configuration as a trap for electrons (Fig. 9 [126, 127]). Then, in contrast to the cathode processes for glow discharge, ionization in magnetron discharge results from bombardment of the cathode surface with ions which must obtain an energy of hundreds of eV from the electric field. Collisions of ions of such an energy with a surface is accompanied by emission of atoms from the surface. Hence, cathode erosion

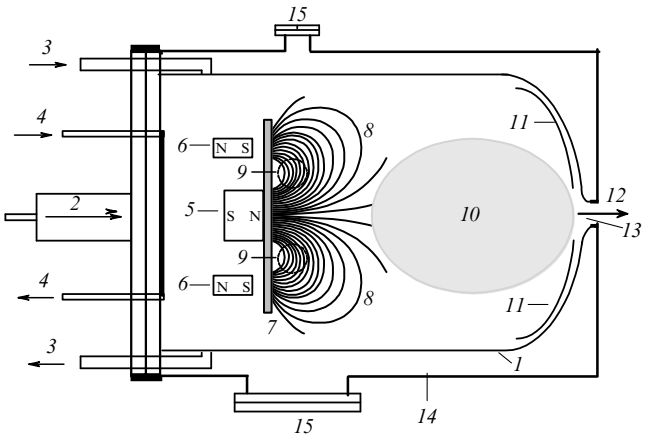

Figure 9. Schematic of magnetron generator of clusters [126, 127]: *1* — aggregation camera, *2* — flow of the buffer gas, *3* — liquid nitrogen for chamber cooling, *4* — water cooling of the magnetron. Two cylindrical magnets (*5*, *6*) create a magnetic field above the cathode (*7*) with the maximum of the magnetic field strength in the region between the magnets. Electrons are captured by the magnetic field and are located in the region of the field strength maximum, and the magnetic field barely acts on the ions. The ions bombard the cathode and create secondary electrons, which partially reach the cathode and bombard it. *8* — lines of magnetic force, *9* — a ring of trapped electrons (track), *10* — secondary plasma, *11* — secondary plasma electrode, *12* — flow of a buffer gas with clusters, *13* — discharge nozzle, *14* — vacuum region, *15* — pumping.

under the action of magnetron discharge is a secondary process, which does not determine the ionization balance. But just the character of the ionization equilibrium in magnetron discharge makes it effective in the generation of metal atoms.

The cathode region of magnetron discharge is one between the traps for electrons and the cathode. The charge of this region is created by ions bombarding the cathode, and also by secondary electrons which leave the cathode. Since the total electric current to the cathode due to the ionization equilibrium is practically zero, and the typical ion velocity is small compared to the electron velocity, the charge in the cathode region is determined by ions. Ultimately, the excess charge in the cathode region creates an electric field which compensates the external field. The cathode layer depth l follows from the three-halves Child–Langmuir law [128, 129], which connects the current density i, the electric potential of the cathode layer U, and its thickness l by the formula

$$i = \frac{2}{9\pi}\sqrt{\frac{e}{2m_\mathrm{i}}}\,\frac{U^{3/2}}{l^2}\,, \tag{3.24}$$

where m_i is the ion mass. For typical values of the current density $i \sim 10$ mA cm^{-2} in magnetron discharge and voltages $U \sim 300$ V, we have for the cathode layer thickness $l \sim 0.2$ mm in argon. This corresponds to a high electric field strength in the cathode region of the order of 10^4 V cm^{-1}.

From this, an important requirement follows for the magnetron discharge as an atom generator. It is necessary for an ion to reach the cathode with the electrical energy eU without collisions with buffer gas atoms in the course of its propagation. Therefore, the number density N of buffer gas atoms is restricted in accordance with the criterion

$$N\sigma l \ll 1\,, \tag{3.25}$$

where σ is the diffusion cross section of ion-atom scattering, and l is the thickness of the cathode layer. In particular, let us assume for argon as a buffer gas that resonant charge exchange is responsible for ion-atom scattering, and the cross section of this process is $\sigma_\mathrm{res} = 3.9 \times 10^{-15}$ cm^2 at the collision energy of 100 eV [130]. Since the diffusion cross section of ion-atom scattering σ^* is connected in this case with the cross section of resonant charge exchange by the relation $\sigma^* = 2\sigma_\mathrm{res}$ [131], we obtain on the basis of criterion (3.25) $N \ll 5 \times 10^{15}$ cm^{-3}, i.e., magnetron discharge is realized at low pressures of the buffer gas.

The method of generation of magnetron discharge to generate metal clusters has been worked out and developed by H Haberland et al. [132–138]. Figure 9 gives a typical scheme of the magnetron chamber, where magnetron discharge is the generator of metal clusters. In the bombardment of the cathode in the magnetron discharge with ions, a flux of metal atoms occurs in the chamber, through which the buffer gas flows. As a result of collisions with buffer gas atoms, metal atoms are thermalized and then join in clusters. These clusters grow in the course of their transport in the buffer gas, and then they leave the aggregation chamber together with the buffer gas flow. A typical metal cluster includes tens of thousands of atoms at the exit.

Let us consider the peculiarities of cluster generation in a magnetron discharge. The transition from free metal atoms to clusters in the magnetron chamber in the course of cluster growth is described by the following scheme [139–141]:

$$2M + A \longrightarrow M_2 + A\,, \quad M_n + M \longrightarrow M_{n+1}\,. \tag{3.26}$$

Here, A is an atom of the buffer gas, and M is a metal atom. The three-body process is the slowest one in this scheme, which leads to the formation a diatomic metal molecule, which subsequently becomes a condensation nucleus in pair processes of cluster growth and characterizes the number of clusters up to a given time. The rate constant of the three-body process in this scheme is estimated as $K \sim 10^{-33}$ cm^6 s^{-1}, and below we use for this rate the constant $K = 3 \times 10^{-33}$ cm^6 s^{-1} [127]. In estimating a typical time of conversion of a metal vapor inside a buffer gas into a gas of clusters, we take into account that atom attachment to clusters proceeds fast compared to the three-body process of formation of new condensation nuclei.

Based on experimental data and estimations [127, 142], we take the following parameters of the magnetron plasma. The number density of buffer gas (argon) atoms is $N = 4 \times 10^{15}$ cm^{-3}, and the relative concentration of the metal atoms is 1%, i.e., a typical number density of metal atoms is $N_\mathrm{m} = 4 \times 10^{13}$ cm^{-3}, and the average number of atoms in the cluster is $n = 3 \times 10^3$. This gives a typical time of cluster formation of

$$\tau_\mathrm{cl} \sim \frac{1}{NN_\mathrm{m}Kn} \sim 1\ \mathrm{s}\,. \tag{3.27}$$

This time is comparable to the drift time of metal atoms and metal clusters in the aggregation chamber.

Let us compare this time τ_cl with the time of atom departure to the walls of the aggregation chamber. A typical value of the diffusion coefficient of metal atoms in argon under normal conditions is $D_\mathrm{m} \sim 0.1$ cm^2 s^{-1}, which corresponds to the diffusion coefficient $D_\mathrm{m} \sim 10^3$ cm^2 s^{-1} at a typical pressure inside the chamber. From this, it follows for

a typical time of attachment of metal atoms to the aggregation chamber walls that

$$\tau_D \sim \frac{r^2}{2D} \sim 0.04 \text{ s}, \tag{3.28}$$

where $r = 5$ cm is the radius of the aggregation chamber. It should be noted that formula (3.27) gives an understated value for a typical time of cluster growth, because this process starts after thermalization of metal atoms, and formula (3.28) leads to an overestimated transport time to the walls, because metal atoms are located at the beginning at different distances from the walls of the aggregation chamber.

Thus, it follows that the magnetron generator of metal clusters requires a low gas pressure which does not exceed 10^{-4} atm. On the other hand, at low pressures, metal atoms attach to the chamber walls after thermalization without conversion into clusters. This leads to a low efficiency of atom conversion in clusters. This efficiency may be increased by using a pulse regime of magnetron discharge, in accordance with the Hippler concept [143]. According to this concept, it is profitable to input an electric energy of continuous magnetron discharge during a short time period, and after the pulse one can increase the pressure in the magnetron chamber several times as a result of injection of a buffer gas into the chamber. As a result, the rate of cluster formation and growth increases several-fold, as does the typical time of transport of metal atoms to the walls, which corresponds to an increase in the efficiency of transformation of a metal vapor into a gas of clusters. During the time between successive pulses, the gas pressure in the chamber returns to its initial value due to the flow of the buffer gas with clusters through the orifice. The efficiency of conversion of metal vapor atoms into clusters is less than 1% for the continuous regime, whereas in pulsed magnetron discharge this efficiency may be increased to several percent.

In spite of the low efficiency of metal vapor conversion into a gas of clusters in a magnetron discharge, this method is the most widely used in studies with intense cluster beams. This is partially due to the large area of the cathode, which leads to high discharge currents and intense cluster beams. However, the main advantage of this method results from industrial production of the setup for NC200 generators of metal cluster beams by Oxford Applied Research (United Kingdom) [144], which allows one to obtain beams of metallic clusters, as they say, 'from the outset.' For this reason, at present, most investigations with intense beams of metal clusters are fulfilled on the basis of magnetron cluster generators.

3.3 Evaporation of microparticle in a buffer gas flow

The first stage of the formation of nanostructures is the generation of a dense metal vapor. Subsequently, this vapor is transformed into nanoclusters, and when the nanoclusters become solid, they join into fractal structures. As shown above in Section 3.2, the efficiency of formation of metal clusters is small when using a bulk metal, the surface of which is excited by a plasma beam or a laser beam if most of the input energy is expended in this case on sample heating. This may be avoided if a bulk sample is replaced by a microparticle, as used in plasma chemical processes [145–147]. This method is suitable for generating intense beams of metallic clusters [148, 149].

An efficient method for generating fractal fibers is described in [149], where a metal microparticle is suspended

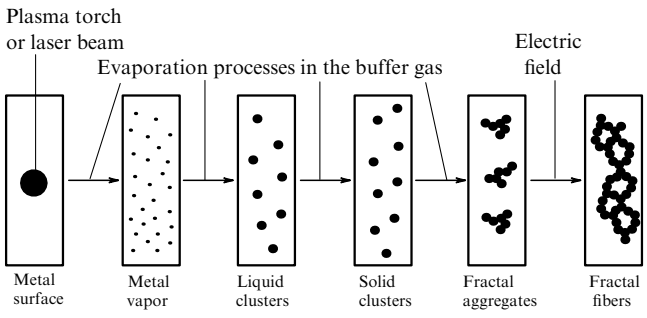

Figure 10. Processes of formation of fractal fibers as a result of irradiation of a metal surface by a laser beam or a plasma torch [151]. The sequence of the processes given above and intermediate objects are listed underneath [149].

in the flow of a buffer gas and is heated by the action of an external plasma source or electromagnetic waves. Vaporization of this particle leads to the formation of a metal vapor that is captured by the buffer gas flow. As a result of subsequent processes involving metal atoms in the buffer gas [150], metal clusters are formed and are then converted into fractal aggregates which, in turn, are joined into fractal fibers, if the growth process takes place in an external electric field.

The corresponding sequence of processes in the formation of metallic nanostructures, in particular, fractal fibers, is shown in Fig. 10. Because of the high density of the metal vapor in a small region of space, growth processes of fractal structures occur fast up to the formation of fractal aggregates and proceed in the course of the buffer gas flow drift. A similar sequence of formation of metal nanostructures is realized under the action of intense pulse energy flows in a plasma torch or a laser beam, as was analyzed above in Section 3.2. The regime under consideration for the interaction of energy fluxes and a flat metal surface corresponds to larger pulse times than the typical time of equilibrium establishment between the energy flux and the surface. In addition, the pulse duration is long compared to the time of heat transfer in the metal in the region of absorption of electromagnetic waves. This scheme was used in the first experiment by Lushnikov et al. [74] to generate fractal metal fibers.

The first stage of the process chain given in Fig. 10 in the generation of metal nanostructures is the formation of a metal vapor in a buffer gas. Atoms of the vapor are then joined into clusters, i.e., nanoparticles consisting of bound metal atoms. Further solid clusters are joined into fractal aggregates, a rarefied metal structure whose density decreases as it grows, so that at micron sizes it becomes unstable. Upon subsequent growth, the structure density does not depend on its size, but the growth rate of the structure drops sharply with its increase. The last stage of the chain of processes given in Fig. 10 leads to the formation of fractal fibers if this process takes place in an external electric field. In the absence of an electric field, an isotropic fractal structure is formed as a result of the growth process. Although an external electric field significantly accelerates the growth process, the last stage is long. Roughly, the duration of the first stages of the process sequence shown in Fig. 10 is seconds, while the formation of fractal fibers is measured in minutes.

The main difference between this method of generation of fractal fibers [149] and the above ones is that the metal particle is 'suspended' in the buffer gas flow, and evaporated metal

atoms are captured by this flow, so that the nucleation process with the formation of metal clusters proceeds in the gas flow. Therefore, all the evaporated atoms are finally transformed in solid clusters. In the case of a metal surface, evaporated atoms are distributed over the volume occupied by a buffer gas, and therefore a certain part of them attaches to the chamber walls, decreasing the efficiency of generation of the fractal fibers.

Processes of generation of metal nanoclusters and nanostructures within the framework of the above scheme are represented in Fig. 11. In this scheme, a metal microparticle is thrown into a buffer gas flow, and the captured particle hangs in a conical chamber at a point where the particle weight becomes equal to the frictional force from a gas flow directed upwards. Vaporization of this particle proceeds under the action of an external energy source, for which a high-frequency discharge or a laser beam may be used. Further clusters are formed in a region of a lower temperature and, when they become solid, their association leads to the formation of fractal aggregates. If fractal aggregates are located in an external electric field, as is the case in the above scheme, fractal aggregates join into fractal fibers in the end.

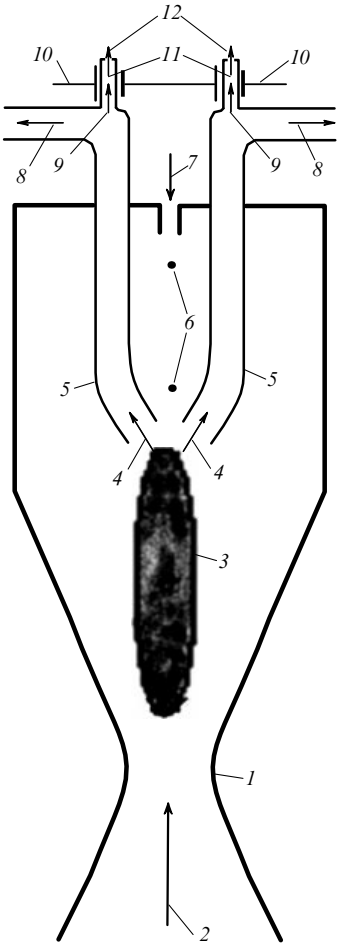

Figure 11. Schematic of generation of metal nanostructures from a metal microparticle heated by an external energy source and located in an argon flow [149]. *1* — aggregation camera, *2* — argon flow, *3* — region of energy input from an external energy source, *4* — current lines for an argon flow with a metal vapor and clusters, *5* — tube for propagation of the argon flow, *6* — falling microparticles, *7* — orifice for injection of microparticles, *8* — flow of the gas to the pumps, *9* — argon flow with metal clusters and aggregates, *10* — electric field, *11* — region of growth of fractal structures, *12* — flow of excess argon.

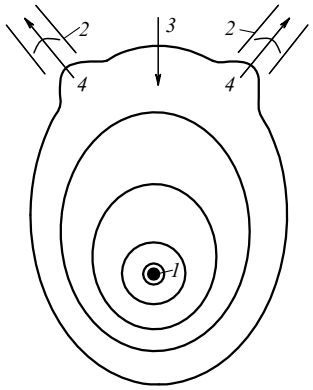

Figure 12. Positions of isotherms in an argon flow near a hot metal microparticle in the flow plane [149]. *1* — microparticle *2* — tubes, *3* — particle injection, *4* — argon flow.

Positions of isotherms are represented in Fig. 12 for a flow around a microparticle heated by an external power source in accordance with the schematic in Fig. 11. Though a high surface temperature of the microparticles causes their vaporization in an argon flow, the temperature drops as the distance from the particle increases. Therefore, already close to the particle surface a temperature is established at which the nucleation process proceeds, which is accompanied by energy release. Nevertheless, because of the high metal vapor density, the process of metal vapor conversion into clusters finishes near the microparticle. Further, small metal clusters are joined into larger ones as a result of a coagulation process resembling the joining of liquid drops. This process finishes in a flow region, where the clusters become solid. Subsequent joining of solid nanoclusters into fractal aggregates and further into fractal fibers is not shown in Fig. 12.

Table 5 compares parameters of the generation of metal clusters and nanostructures consisting of them in the cases of the magnetron method and the method of vaporization of a microparticle. In this comparison, we are guided by the silver case. The energy cost to form a single atom in the magnetron method is the product of the ion energy in the magnetron discharge upon cathode bombardment and the probability of atom production as a result of release from the cathode surface, whereas this value resulted from atom evaporation from the microparticle surface due to its high temperature slightly exceeding the atom binding energy in the metal. Almost all the evaporated metal atoms are converted into clusters in the method of microparticle vaporization because of the high vapor density, while most of the metal atoms go to the walls of the chamber in the magnetron method of aggregation. Next, nucleation processes in the method of

Table 5. Metal vapor formation parameters of the first stage of generating nanostructures of silver by magnetron discharge and by evaporation of a metal microparticle in a buffer gas flow.

Parameter	Magnetron discharge	Microparticle vaporization
Cost of atom formation, eV	500	4
Probability of atom conversion	0.01	1
Drift time, s	1	0.01
Nucleation time, s	1	10^{-6}
N_m, cm^{-3}	10^{13}	10^{17}
Size of nucleation region, cm	5	0.01
Intensity of cluster beam, μg s^{-1}	—	30

microparticle vaporization proceed in a small region and at a higher density of metal atoms N_m than in the magnetron method. As a result, a microscopic amount of metal is formed in clusters and nanostructures.

4. Processes in a buffer gas with metal nanostructures

4.1 Propagation of gas flow through a fractal structure

Metal nanostructures have an application interest in two senses. If this structure is used as a catalyst or a filter, a buffer gas with an impurity of reacting or dopant molecules propagates through the structure. Then the first stage of the process is the attachment of active molecules to the nanostructure, which depends on the gas dynamics of flow propagation through a rarefied structure. Another application involves the use of a metallic nanostructure as a conductor of a conductometric sensor, i.e., a device that allows the presence of impurities to be measured in gas flows on the basis of varying the electrical resistance of the metal nanostructure which results from attachment of active molecules to the nanostructure. Below, we analyze the character of processes in these cases.

Let us consider the propagation of a buffer gas flow with impurity molecules through a cylindrical tube which is filled with a metal nanostructure. Active molecules of the flow may then attach to the surface of solid clusters which constitute this structure and partake in subsequent processes in such a form. This allows one to use the metal structure as a catalyst or filter, and buffer gas molecules collide with clusters, which constitute elements of the nanostructure. As a result of interaction with the nanostructure, the buffer gas flow decelerates. Below, we estimate the resistance from a metal nanostructure to a gas flow.

Let the radius of the cylindrical tube filled with a nanostructure be R. The distribution of the flow velocity along the tube radius is given by the Poiseuille formula [110]

$$v(r) = u\left(1 - \frac{r^2}{R^2}\right), \tag{4.1}$$

where u is the gas flow velocity at the tube center, and r is the distance from the tube's axis. The gas pressure gradient occurs in the course of flow propagation in accordance with equation [110]

$$\frac{\mathrm{d}p}{\mathrm{d}z} = \frac{4\eta u}{R^2}, \tag{4.2}$$

where z is the coordinate directed along the tube, and η is the gas viscosity coefficient. For a tube of length l, we have for the pressure difference Δp at the tube ends

$$\Delta p = \frac{4\eta l}{R^2 u}. \tag{4.3}$$

The pressure variation at the tube ends is relatively small:

$$\Delta p \ll p. \tag{4.4}$$

We now consider the case when a metal nanostructure is located inside the tube. The mean free path of molecules in atmospheric air is about 100 nm at atmospheric pressure, while the size of solid clusters constituting a metal nanostructure is smaller, being a few nanometers. Therefore, the scattering of atoms or molecules of a buffer gas on the metal nanostructure is reduced to scattering of these atoms or molecules on individual clusters of the nanostructure. From this, it follows that arresting the gas flow with a metal nanostructure does not depend on the type of nanostructure, but is determined by the cluster density. In other words, the subsequent conclusions apply equally to both aerogels and fractal fibers consisting of metal clusters.

Since a solid cluster of the fractal structures can interact with only a single atom or molecule of a buffer gas at each time, the force acting on the gas flow from one cluster of the nanostructure is [105, 152]

$$F = v\,\frac{8\sqrt{2\pi m T}}{3}\,Na^2. \tag{4.5}$$

Here, v is the flow velocity at a given point, m is the mass of a buffer gas atom, T is the gas temperature expressed in energy units, N is the number density of gas atoms, and a is the cluster radius. This force acts in the opposite direction with respect to gas movement, and formula (4.5) requires the validity of the following criterion:

$$v \ll v_T, \quad v_T = \sqrt{\frac{8T}{\pi m}}, \tag{4.6}$$

where v_T is the average thermal velocity of buffer gas atoms.

Averaging the frictional force over the tube cross section gives

$$F = u\,\frac{4\sqrt{2\pi m T}}{3}\,Na^2, \tag{4.7}$$

where u is the flow velocity at the tube center. As is seen, the fractal structure creates an additional resistance force to the gas flow. The model where resistance is created by a system of independent clusters and formula (4.7) gives the braking force to a gas flow from one cluster. Evidently, the same force acts on an individual cluster of the nanostructure. This gives the frictional force acting on a unit volume of a gas flow that propagates through the nanostructure, $N_{cl}F$, where N_{cl} is the number density of clusters of the nanostructure. Hence, by the definition (or from the Euler equation) we obtain a gas pressure gradient in the flow under the action of the nanostructure:

$$\frac{\mathrm{d}p_{cl}}{\mathrm{d}z} = -N_{cl}F = -u\,\frac{4\sqrt{2\pi m T}}{3}\,N_{cl}a^2. \tag{4.8}$$

If the nanostructure is distributed uniformly in a layer of thickness l, its presence leads to an additional pressure drop in the tube Δp_{cl} in accordance with the formula [149]

$$\Delta p_{cl} = \frac{4\sqrt{2mT}}{3\sqrt{\pi}}\,u\xi, \tag{4.9}$$

where $\xi = N_{cl}\pi a^2 l$ is the filling parameter for the nanostructure in the tube according to formula (2.7). From this, we obtain the relative change in the gas pressure in the tube due to the presence there of a fractal structure:

$$\frac{\Delta p_{cl}}{p} = \frac{16}{3\pi}\,\frac{u}{v_T}\,\xi, \tag{4.10}$$

where the parameter ξ is defined by formula (2.7), and the pressure p for an ideal gas is given by $p = NT$. Since $u \ll v_T$ and $\xi \ll 1$, we obtain a relatively small change in the gas flow pressure inside the tube $\Delta p_{cl} \ll p$ due to the presence of metal nanostructures inside it.

The system under consideration, where a buffer gas with an impurity of active molecules propagates through a metal nanostructure, is used for chemical reactions in a gas with a nanostructure as a catalyst. Then, a reacting molecule attaches to the nanostructure and partakes in a chemical process in such a form. The parameter of this process is the number of collisions v for an impurity molecule with the nanostructure in the process of a buffer gas passage with impurity molecules through the nanostructure. Assuming for simplicity that each collision leads to the attachment of a molecule, we conclude that the catalyst must satisfy the criterion $v \gg 1$.

In evaluating the parameter v, we assume, as above, that a buffer gas flow propagates through a tube of a length l. A metal nanostructure, which is characterized by the filling parameter ξ, is found inside the tube. Let us determine v as the product of the drift time of a gas flow through the tube with the nanostructure $\tau_p \sim l/u$ and the frequency of collision of a test molecule with a nanostructure skeleton $1/\tau_{at} \sim \pi a^2 N_{cl} v_T$, which gives

$$v \sim \frac{\tau_p}{\tau_{at}} \sim \frac{v_T}{u} \xi . \tag{4.11}$$

Let us estimate the effective length L of the fractal structure under the condition that it significantly exceeds the mean free path of molecules in the buffer gas. Under this condition, each molecule is slowed as a result of the collisions with a skeleton of the fractal structure. According to formula (4.11), if $\xi \sim u/v_T$, the probability of molecule collision with a skeleton of the fractal structure or the probability of attachment of a test molecule to it is of the order of unity. This structure can further be used as a catalyst. Note that the interaction of a gas flow with different types of nanostructures, such as an aerogel or fractal fiber, occurs in the same manner through interaction with solid clusters as elements of these structures. This means that a parameter of fractal structures is the density of solid clusters. However, the formation of fractal fibers in an external electric field proceeds faster than aerogels [106, 96]. Therefore, considering the behavior of fractal structures in gases, we are guided by fractal fibers.

4.2 Resistance of a metal nanostructure

A conductor is the basis of a conductometric sensor, and its work consists of measuring the electrical resistance of the conductor. The change in the electrical resistance of the conductor as a result of attachment of active molecules to the conductor surface is measured. A variation in the electric current through a conductor is the yield sensor parameter and, according to [153], the industrial electrometer 6517A allows one to measure simultaneously currents in the range of $10^{-13} - 0.02$ A, as well as to determine the voltage in the range of $10^{-5} - 200$ V. Below, being guided by numerous measurements [154], we take the sensor current in the range of $10^{-9} - 10^{-6}$ A, and the voltage of 1 V, so that the conductor resistance is concentrated in the range between 1 kΩ and 1 MΩ. In addition, we will be guided by the distance between the electrodes of $l = 1$ cm. We use these parameters below to evaluate sensor parameters.

Though it is impossible to prepare a metal wire with a radius of less than 10 μm, we first consider as a model conductor a piece of metal cylindrical wire of a smaller radius. In calculating the resistance of the metal system used as a conductor, we use as our basis the simplest metal model — the Bethe–Sommerfeld model [155], which considers a metal electrons as a degenerate electron gas. In this case, the metal conductivity is determined by electrons located near the Fermi surface in the space of the electron momenta, and the distribution function of valence electrons in this energy range is given by the Boltzmann formula. Accordingly, the conductivity of the metal Σ within the framework of this model is given by [156, 157]

$$\Sigma_0 = \frac{1}{\rho_0} = \frac{N_e e^2 \tau}{m_e} , \tag{4.12}$$

where N_e is the number density of valence electrons partaking in the creation of the metal conductivity, e is the electron charge, τ_s is a typical time of electron scattering on inhomogeneities located inside the metal, and m_e is the effective mass of electrons inside the metal, which we identify with the free electron mass.

The parameters of formula (4.12) are given in Table 6. The values of the specific resistance of metals $\rho_0 = 1/\Sigma_0$ at room temperature are taken from [109], the values of electron velocities on the Fermi surface v_F [109, 158] are used as typical electron velocities v_e in formula (4.12), where the valence electrons of the atoms are considered as conductive electrons, and their number density N_e [109, 158] is used as the number density of conductive electrons. Note that the values of the electron number density in metals obtained on the basis of measurements of the Hall constants exceed those given in Table 6 by 20–50%. The values of a typical scattering time τ_s, given in Table 6, are determined on the basis of formula (4.12) and the data in Table 6. From this, we have for the resistance R_0 of the conductor under consideration

$$R_0 = \frac{\rho_0 l}{\pi r^2} , \tag{4.13}$$

where r is the cylinder conductor radius. Table 6 also contains values of the minimum r_{min} and maximum r_{max} radii of conductors of these metals, consisting of truncated balls, so that the above range of wire resistance 1 kΩ–1 MΩ corresponds to a radius of the cylinder conductor in the range between r_{min} and r_{max}. As is seen, we are dealing with nanometer conductor transverse sizes, i.e., such a conductor cannot be prepared in the wire form.

Because it is impossible in reality to create a cylinder conductor of laboratory sizes with a diameter of less than 10 μm, nanostructures are used for this goal. In this case, a

Table 6. Resistance parameters of a cylindrical metal wire 1 cm in length with a resistance between 1 kΩ and 1 MΩ at room temperature.

Parameter \ Metal	Fe	Cu	Ag	Au
ρ_0, 10^{-8} Ω m	9.98	1.72	1.63	2.27
Σ_0, 10^{17} s^{-1}	0.9	5.2	5.5	4.0
N_e, 10^{22} cm^{-3}	17	8.5	5.9	5.9
v_F, 10^8 cm s^{-1}	2.0	1.7	1.4	1.4
τ_s, 10^{-14} s	0.21	2.4	3.7	2.7
r_{min}, nm	18	7.4	7.2	8.5
r_{max}, nm	560	230	230	270

conductive channel is modeled by a broken line with a length of an elementary segment of the order of nanometers, so that considering a nanostructure to be a conductor for the sensor, it is necessary to modify the above formulas obtained for a cylindrical conductor. Following this, we first consider a percolation cluster as a sensor conductor, the most studied nanostructure from the standpoint of the passing of an electric current through it. A specific feature of the percolation cluster distinguishing it from other nanostructures is its preparation by placing nanoclusters on the surface in a random manner, which corresponds to the real process of its formation by deposition of solid metal nanoclusters on a dielectric substrate.

An example of such a percolation cluster is given in Fig. 13. The size of the grains in the final structure is slightly higher than the initial cluster size as a result of processes involving these clusters on the surface during their attachment. Next, in estimating the electric parameters of the percolation cluster, we assume for definiteness that it consists of individual grains of a radius of 30 nm, in accordance with Fig. 13. Evidently, at a certain number density of clusters on the surface, a conductive channel is created between the boundaries of the region in which clusters are deposited. This cluster density is called the percolation threshold [161],

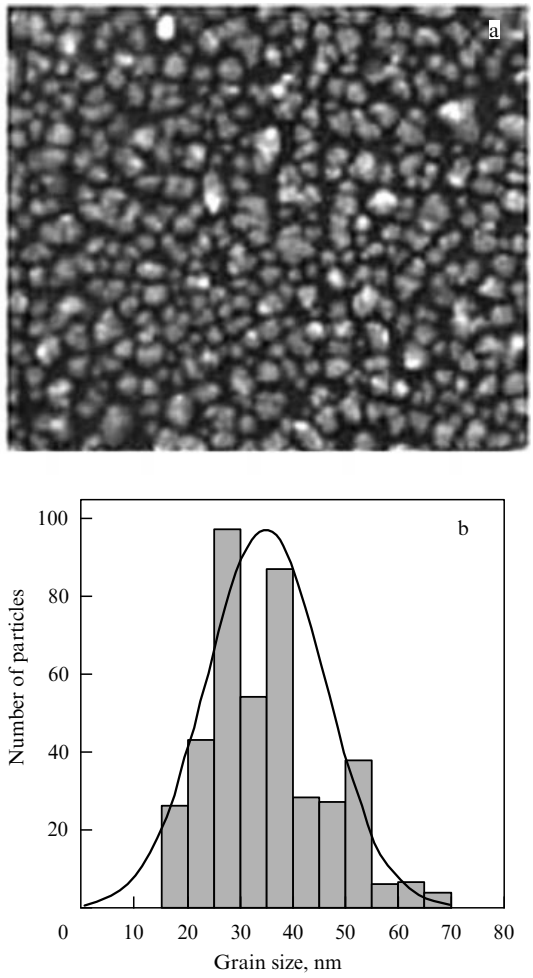

Figure 13. Example of the formation of a metal coating during the deposition of silver nanoclusters onto a silicon substrate [159, 160]. (a) Photograph of the surface structure obtained with a TEM (microscope with a transmitted electron beam), (b) size distribution of the sputtered clusters.

and we will consider the range of cluster densities on the substrate above the percolation threshold, but close to it. In this case, there are a restricted number of channels through which the electric current can pass, if the electrodes are boundaries of the percolation cluster.

Our task is to determine the resistance of a percolation cluster, the elements of which are grains modeled by balls bonded with each other. Therefore, the conductive channel has a variable cross section along it. Let us estimate the error in modeling the conductive channel by a broken line of a constant cross section, i.e., if elements of this structure consisting of truncated balls are replaced by cylinders. In particular, an element of the structure under consideration, which includes three nanocluster-balls located for simplicity on one line, is given in Fig. 14. Our task is to estimate the variation of this element resistance R in replacing it by a cylinder of the same length with a resistance R_0. If the radius of an individual ball is r, and the radius of the straight arch between neighboring balls equals a, the ratio of these resistances is given by

$$\frac{R}{R_0} = \frac{1}{2t} \ln\left(\frac{1+t}{1-t}\right), \tag{4.14}$$

where $t = \sqrt{1 - a^2/r^2}$, and in the limit of $a \to r$ this ratio is equal to one. According to this formula, at $a = 0.5r$ this ratio is $R/R_0 = 1.5$, and at $a = 0.3r$ the resistance ratio is $R/R_0 = 2$. Below, we use the model, replacing the elements of the percolation cluster, which is a system of bound balls, by a system of cylindrical fibers. Therefore, we model the percolation cluster as a system of elements of a cylindrical shape, and taking its resistance within the framework of this model, one can estimate its accuracy as ~ 2.

Let us consider geometric peculiarities of the two-dimensional percolation cluster. Let the two-dimensional percolation cluster be located between two parallel plates separated by distance l. Then, the conductive channel length of the percolation cluster is given by [162]

$$L = 1.5r\left(\frac{l}{r}\right)^{1.15}, \tag{4.15}$$

where for simplicity we assume on average $a = 0.5r$, where a is the radius of the straight arch between cluster-balls. Since this formula (4.15) is considered an estimate, we omit below the coefficient 1.5. This formula takes into account that the conductive channel is a broken line which connects conductive plates. Some points of the conductive channel may be then connected with multiple lines. In determining the resistance, we retain only those pieces of the conductive

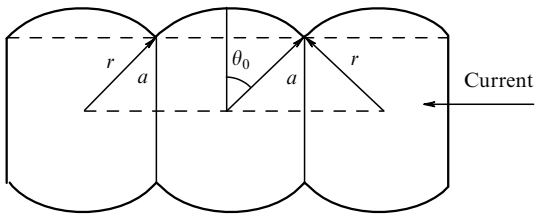

Figure 14. Model of an element of a metal nanostructure consisting of bonded solid clusters which are modelled by a system of truncated balls. This system is compared with a cylindrical piece of wire of the same material, radius, and length.

channel whose points can be connected by only one broken line, i.e., the current can flow in only one segment of these sites. The length of this channel part that connects the conductive plates is [161, 163]

$$L' = r\left(\frac{L}{r}\right)^{0.75}. \tag{4.16}$$

Notably, if the distance between the plates is $l = 1$ cm, formulas (4.15) and (4.16) give for the total length of the conductive channel $L = 7$ cm and the length of the channel part with a greater resistance is $L' = 0.2$ cm. On the basis of formulas (4.15) and (4.16), we have the following expression for the minimum resistance of the percolation cluster R_{th} at the percolation threshold if there is only one path for the current flow between the plates:

$$R_{\text{th}} = \frac{\rho_0 L'}{\pi r^2} = \frac{\rho_0}{\pi r}\left(\frac{l}{r}\right)^{0.86}, \tag{4.17}$$

where ρ_0 is the specific metal resistance at $T = 300$ K, whose values [109] are given in Table 6. Table 7 contains values of the threshold resistance R_{th} under the conditions of Fig. 13, with an average radius of individual grains of 30 nm. In addition, values of the threshold currents through this percolation cluster are given in Table 7 at the percolation threshold for the voltage $U = 1$ V between the plates.

Note the strong dependence of the minimum resistance $R_{\min}$ of the percolation cluster on the radius of its constituent elementary nanoclusters. For example, if the percolation cluster consists of individual nanoclusters of a radius $r = 5$ nm instead of the above value $r = 30$ nm, we find that the minimum resistance in accordance with the previously used formulas increases 28-fold. In addition, ignoring the contribution of regions between grains of the conductive channel to its resistance, when the electric current can propagate along several paths, we have an underestimated value for the resistance of the percolation cluster. Nevertheless, the obtained values for its threshold resistance are in accord with the above parameters of the electrical circuits. Note that to practically provide the minimum resistance of the percolation cluster, it is necessary to measure the electric current between the conductive plates in the course of nanocluster deposition on a substrate and to stop the spraying process, as soon as the electric circuit with the percolation cluster starts, i.e., as the electric current between plates is detected.

Within the framework of the standard scheme for a conductometric gas sensor with a conductor as its basis, the presence of active molecules in a buffer gas is detected by variation of the conductor resistance. In this case, the conductor is the percolation cluster, and active molecules form negative ions on the surface. Since the conductor is an absorber of active molecules, it is convenient to roll it into a tube, through which a buffer gas with active molecules passes. Initially, the percolation cluster is located between two flat metal plates which are rolled into rings as the ends of the conductor, and the surface on which the percolation cluster is located initially is converted into a cylindrical tube with a conductor on its inner surface.

Table 7. Parameters which are used for evaluation of the resistance change of the metal conductor as a result of attachment of NO_3 molecules to the metal surface, which are converted there into negative ions.

Parameter \ Metal	Fe	Cu	Ag	Au
W, eV	4.3	4.4	4.3	4.3
Σ_0, 10^{17} s^{-1}	0.9	5.2	5.5	4.0
σ_e, nm^2	2.1	2.1	2.6	0.76
A, 10^3	1.5	7.4	7.9	1.7
$n_{\min}$, 10^6 cm^{-2}	100	3.7	3.3	21
R_{th}, kΩ	60	10	9.7	14
I_{th}, μA	17	100	100	70

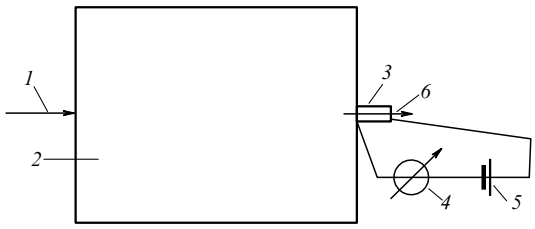

Figure 15. Character of the sensor action. *1* — input, *2* — chamber with a buffer gas, *3* — sensor, *4* — ampermeter, *5* — battery, *6* — flow of the buffer gas current with active molecules.

In the course of the sensor work, a current is measured between the two rings; Fig. 15 represents the measurement circuit in this case. In this scheme, the sensor-tube is the inner surface of the chamber to which active molecules attach. In the course of measurements, a buffer gas with active molecules flows through this tube as through an orifice.

Note that in the scheme under consideration, where the percolation cluster is used as the conductometric gas sensor, the electric current flows through a small part of the metal structure. This testifies to the low efficiency of the metal used in this scheme. Indeed, let us go to the limit, where clusters deposited on the surface form a single layer, i.e., the conductive surface becomes continuous. At a typical distance between the electrodes of 1 cm, a radius of the sensor tube of 3 mm, and a diameter of grain-clusters on the surface of 30 nm, in accordance with Fig. 13 we obtain the resistance of this layer to Table 6 metals less than 1 Ω instead of the postulated one in Table 6 values of the conductor resistance between 1 kΩ and 1 MΩ. This means that it is practically necessary to reduce the resistance of the metal coating by several orders of magnitude, and this corresponds to transition to the percolation threshold. In this case, a small part of surface metal clusters is included in the conductive channel, which indicates the low efficiency of the metal used in this sensor.

Unfortunately, we have no information about which part of the material does not participate in the transfer of the sensor electric current for other types of conductometric gas sensors. This may be judged by the average number of nearest neighbors which are in contact with the test cluster. For the percolation cluster near the percolation threshold, the number of nearest neighbors is fewer than 2; if the surface is completely filled with one layer and clusters form a square lattice, this value is 4; and for the hexagonal lattice this equals 6. In the case of a DLA-cluster, the average number of nearest neighbors is approximately 2.25 [164] if the sticking probability as a result of contact between attached solid clusters in the course of deposition is one. One can add to this that, in spite of the low efficiency, the percolation cluster is a convenient model in the analysis of the conductive properties of metal nanostructures.

4.3 Resistance of a metal conductor with active molecules on the surface

The subject of the subsequent analysis is a conductometric gas sensor with a conductor as the basis, whose resistance (or conductivity) varies under the action of active molecules located in a buffer gas (for example, [165]). Since the action of molecules is realized near the conductor surface, it is useful to take nanostructures as a sensor conductor, in particular, a bunch of fibers of nanometer sizes [166, 167]. In the sensor based on metallic nanostructures, the percolation cluster [161, 162] can be taken as a conductor, as can fractal fibers [74] or a system bound nanowires obtained in superfluid helium [85–87], because these structures have small cross sections, and methods of their preparation are being developed.

Since active molecules attached to the metal structure affect the metal conductor at a depth of about one nanometer, and the size of a single element of these structures is several nanometers, the metal nanostructures provide the greatest sensitivity for the registration of active molecules which form negative ions on the nanostructure surface. Below, we carry out an evaluation of the change in the resistance of a metal nanostructure under the action of active molecules. We focus on the maximum action of active molecules on the conductor if negative ions are formed on the metal surface. We restrict the consideration to transiting metals, where the transition between the s- and d-electrons promotes the formation of negative ions. Below we consider some aspects of this problem, allowing an understanding of the conditions under which the scheme is realized, as well as an evaluating of the sensor parameters.

The conductometric sensor basically contains a conductor to which detected active molecules attach. This causes a change in resistance of the conductor, which is fixed by the current change flowing through the conductor. In the following analysis, we are guided, for definiteness, by molecules like NO_2 and NO_3, which, notably, are formed during combustion in air. These molecules form negative ions on the metal surface, and the binding energy in the free negative ions is $EA(NO_2) = 2.4$ eV, $EA(NO_3) = 3.7$ eV [168], respectively. The mechanism of the resistance change for the conductor consists of the formation of a positive hole in the metal under the action of a negative ion on its surface. As a result of the Coulomb interaction with a negative ion, an induced positive hole is attracted to the surface. This pair acts as the dipole inside the metal on a valence electron, drifting in an electric field which determines the electric current in the metal system. Such interaction increases the conductor resistance, and the resistance change is proportional to the number of attached active molecules until this change is relatively small.

In evaluating the change in the conductor resistance due to the attachment of active molecules to the metal surface, we first consider the interaction of such molecules with a bulk metal. In the course of this interaction, an attached molecule can capture a valence electron, so that there are two states for a valence electron, as shown in Fig. 16. In the first state, a valence electron remains inside the metal, while in the second state it is captured by the active molecule, which leads to the formation of a negative ion. This causes the formation of a positive hole in the metal that is attracted to the negative ion. Two electron terms are intersected at a distance x_c between them, and at smaller distances between the negative ion and hole, the ionic state becomes the ground state of the system. This distance x_c between an attached molecule and positive

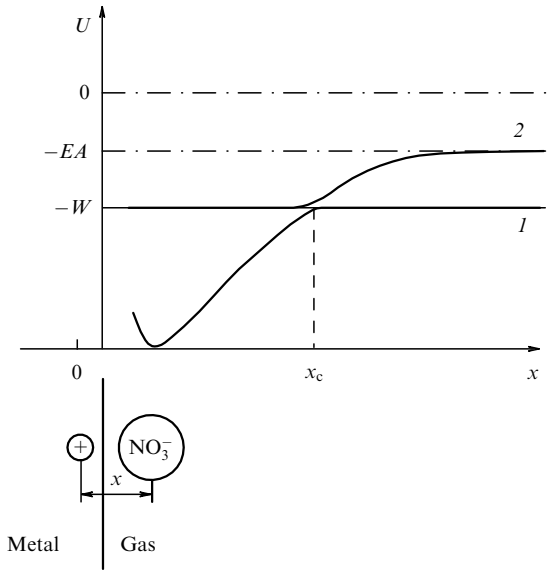

Figure 16. Electron terms of a valence electron for interaction of an NO_3 molecule with a surface metal layer: U is the potential energy for a valence electron, x is the distance between the molecule converted into a negative ion near the metal surface and a positive hole in the metal, W is the metal work function, and EA is the electron affinity to an attached molecule. The electron therm *1* corresponds to a neutral NO_3 molecule interacting weakly with the metal, while the electron term *2* refers to the interaction of the negative NO_3^- ion with a positive hole in the metal.

hole, corresponding to the intersection of electron terms, is given by

$$x_c = \frac{e^2}{W + D - EA}\,, \tag{4.18}$$

where D is the binding energy of an active molecule with the metal surface. Since this value is usually small compared to both the metal work function W and the binding energy of an electron with an active molecule EA, we assume it to be below zero.

Let us analyze the contribution of attached negative ions to the resistance of the metal system. The character of interaction in this case is shown in Fig. 16, so that a surface negative ion attracts a positive vacancy to the metal surface. This pair acts as a dipole on valence electrons, which are located far from them. As a result of charge-dipole interaction, the valence electrons are slowed, reducing the electric current through the metal. The scattering cross section for the valence electron on a dipole σ_e is of the order of x_c^2, so that below we use the following estimation for the scattering cross section of a metal valence electron on a system consisting of a negative ion and a positive hole induced by it:

$$\sigma_e = \frac{e^4}{(W - EA)^2}\,. \tag{4.19}$$

Let us estimate the correction to the sensor conductor resistance due to attached molecules. We represent the specific resistance of this metal system ρ with molecules attached to the metal surface in the form [157]

$$\rho = \frac{1}{\Sigma} = \rho_0 + \Delta\rho\,, \tag{4.20}$$

where ρ_0 is the specific resistance of the metal system in the absence of attached molecules. In accordance with formula (4.12), one can represent the change in the specific resistance of the metal system $\Delta\rho$ due to attached molecules in the form

$$\Delta\rho = \frac{N_m \sigma_m v_e m_e}{N_e e^2} . \quad (4.21)$$

Here, N_m is the average number density of holes inside the metal, whose number is equal to the number of negative ions on the surface, v_e is a typical velocity of electrons, which is taken as the electron velocity at the Fermi surface, σ_e is the cross section of electron scattering on a dipole consisting of a negative ion and a positive hole, and its estimation is given by formula (4.19).

Let us introduce the surface density n_m of molecules attached to the metal surface, which is connected with the average density of positive holes inside the metal N_m by the relation

$$N_m = \frac{2n_m}{r} , \quad (4.22)$$

where r is a radius of the conductive channel. Accordingly, the relative change in metal conductor resistance is

$$\xi = \frac{\Delta\rho}{\rho_0} = Ac_m, \; c_m = \frac{N_m}{N_e} = \frac{2n_m}{rN_e}, \; A = \frac{\sigma_e v_e m_e \Sigma_0}{e^2} . \quad (4.23)$$

Here c_m is the average concentration of positive holes inside the metal induced by negative ions. Table 7 contains some parameters of this formula for the metals under consideration. From this, we also obtain for the average surface density n_{min} of attached active molecules to the conductor surface causing a change to the conductor resistance,

$$n_{min} = \frac{\xi r N_e}{2A} . \quad (4.24)$$

Obviously, the smaller the relative change in the conductor resistance due to attached molecules to it, the lower the accuracy of measurements of this quantity. One can introduce the minimum value of this parameter at which measurements are reliable in accordance with the criterion

$$\xi > \xi_0 = 10^{-6} . \quad (4.25)$$

In accordance with the parameters considered, this corresponds to the minimum measured changes in the resistance $\Delta R = 10^{-3}$ Ω. Table 7 contains the minimal measured values n_{min} of the specific density change in attached molecules to the conductor surface, which provides a reliable measurement of this parameter and is determined by the formula

$$n_{min} = \frac{\xi_0 r_{min} N_e}{2A} . \quad (4.26)$$

Note that the average distance between an attached negative ion and induced positive hole inside the metal is of the order of 1 nm. The average distance between attached negative ions on the metal surface is significantly greater than this value. From this, we have the maximum surface density of negative surface ions of the order of 10^{13} cm^{-2}, which is several orders of magnitude greater than the minimum density of attached molecules, which corresponds to measurable changes in the electric current given in Table 7. Values of the work function W and the specific metal conductivity Σ_0 at room temperature are taken from [109].

5. Applied aspects of metallic nanostructures

5.1 Nanocatalysis

Applications of metal structures relate, in the first place, to the preparation of new materials. These materials are nanostructures of two types: spatial and surface. Previously, fractal fibers and aerogels were considered to be spatial nanostructures. Surface nanostructures may be divided into two groups. In the first one, surface clusters do not interact with each other. These clusters are used as catalysts [169–171]. The surface nanostructures of the second group form a net or web on the surface. In particular, a surface silver nanostructure obtained by deposition of silver clusters on a silicon substrate is represented in Fig. 13 [159, 160]. As a demonstration of the practical importance of these structures, we will focus on this example.

The antiseptic properties of silver have been known for thousands of years [172]. Vessel walls are covered with silver in order to render harmless water or wine located inside the vessel. It is clear that in reality the silver coating kills a certain type of bacteria and can be used as a cure for certain diseases [173–175]. Special studies [176] show that silver surface inhomogeneities of 1–10 nm have the strongest effect on microbes. Because this corresponds to a typical size of clusters, silver clusters on the surface or in a liquid may be used as an antiseptic. In fact, silver clusters are involved in biochemical reactions that kill microbes and delay their growth as a catalyst involved in this process [177]. In this case, the catalytic action of silver clusters for certain types of microbes depends on their size (for example, [178, 179]).

Let us consider as an example the treatment of wounds. The skin protects the body from water and liquid penetration into it, and biochemical processes lead to the healing of wounds. However, microbes delay this process. Silver leads to suppression and destruction of microbes, and thereby silver promotes wound healing. In this case, the silver cluster-particles are introduced into a suspension or ointment, which is applied to a wound. This is one example of the application of materials containing clusters. Some examples will be given below in cluster applications for two areas: catalysts and sensor conductors.

Nanocatalysis [180–182] referred initially to the process involving gold clusters as a catalyst in oxidation of carbon monoxide and hydrocarbons in an air flow. In this case, gold clusters containing about 10 atoms are fastened to the surface of certain metal oxides which are semiconductors. The list of these oxides, semiconductors, providing the process of final oxidation of carbon oxide, is restricted and includes the oxides Fe_2O_3, MgO, TiO_2, CeO_2. The catalytic effect for this process with other compounds used as a substrate is weak. These compounds may be in the form of micron-sized particles, macroscopic solids, or films.

Interestingly, macroscopic gold is a poor catalyst, and even more surprising is that clusters of gold and only gold are such catalysts that enable the oxidation of CO in atmospheric air at room temperature and lower. This effect was discovered by Japanese scientists in 1987 [183, 184, 188], who prepared the catalyst in the form of gold clusters on the semiconductor surface by the chemical method from a solution containing gold compounds. It was shown that the catalytic effect acts

for only small sizes of gold particles on a surface of about 1 nm (the Wigner–Seitz radius [70, 71] for gold equals 0.17 nm). At a diameter above 5 nm of gold particles on the surface, the catalytic effect completely disappears. The optimal size of bound gold clusters on the base corresponds to approximately 10 atoms in a cluster [81, 185–187].

The object and the effect under consideration came to be broadly studied after 2000, both experimentally and on the basis of computer modeling. Studies show the complexity of the catalytic process, where not only the catalyst — a gold cluster attached to a substrate — is of importance, but so is the substrate, which obviously provides oxygen for the chemical process and creates a cluster charge. To fully realize the complexity of the process, let us consider it from general positions of catalytic processes. Let us assume that the catalytic process, the joining of two components, atomic particles B and C, i.e., molecules or radicals, with a catalyst A, proceeds through the formation of a long-lived complex in accordance with the scheme

$$A + B \rightleftarrows AB^{**}\,, \tag{5.1}$$

i.e., a long-lived complex AB^{**} can break, returning the system to its initial state. The chemical process involves a long-lived state

$$AB^{**} + C \to A + BC\,, \tag{5.2}$$

so that the total process corresponds to the scheme

$$B + C \to BC\,. \tag{5.3}$$

Introducing typical times τ_1 and τ_2 for processes (5.1) and (5.2), we learn for probability P that the decay of the long-lived complex AB^{**} leads to the total process (5.3)

$$P = \frac{\tau_1}{\tau_1 + \tau_2}\,. \tag{5.4}$$

If we assume that processes of complex formation have an activation character, i.e.,

$$\tau_1 \sim \exp\left(\frac{E_1}{T}\right), \quad \tau_2 \sim \exp\left(\frac{E_2}{T}\right), \tag{5.5}$$

we can obtain the following temperature dependence for the probability of the chemical process (5.4):

$$P = \frac{1}{1 + A\exp\left(E_\mathrm{a}/T\right)}\,, \tag{5.6}$$

where $E_\mathrm{a} = E_2 - E_1$ is the activation energy of the total process, and A is a numerical coefficient.

Figure 17 shows the temperature dependence of the probability of the catalytic process for CO oxidation in air at given parameters of the air flow through a reactor [81, 185–188], i.e., at a given concentration of CO impurity in air, at a given residence time of the air flow in the reactor, and at a given number of clusters-catalysts on the inner reactor surface for MgO as the surface material. Though the total process

$$2\mathrm{CO} + \mathrm{O_2} \to 2\mathrm{CO_2} \tag{5.7}$$

proceeds with an energy release, the interaction of atomic particles in this process leads to its activation character. Let us

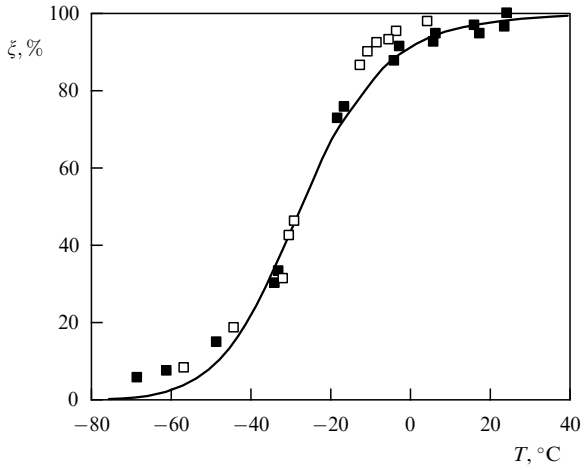

Figure 17. Temperature dependence of the probability of the process $2\mathrm{CO} + \mathrm{O_2} \longrightarrow 2\mathrm{CO_2}$ using a semiconductor $\mathrm{TiO_2}$ as a support and gold clusters fastened to its surface used as a catalyst [189].

treat the data in Fig. 17 on the basis of schemes (5.1) and (5.2) in accordance with formula (5.6). We obtain for the parameters of this formula $E_\mathrm{a} = 0.5$ eV, $A = 6 \times 10^{-11}$. The activation energy corresponds to typical values for chemical processes, but the numerical coefficient for the reversible process of the formation of a long-lived complex in process (5.1) is usually of the order of $A \sim 1$. From this, it follows that the capture of CO molecules by a catalyst is an irreversible process. In this case, this process corresponds to a simultaneous change in the cluster configuration with the attachment of the CO molecule to it and the valence electron transition between different centers.

Let us ascertain how this scheme can be realized for a given process. A free negatively charged gold cluster consisting of 10–20 atoms is characterized by the binding energy of a valence electron in the range between 3 and 4 eV [44]. At this electron binding energy, a tunnel transition with the probability of 6×10^{-11} corresponds to a distance between centers in the range between 1.1 and 1.6 nm [190]. An electron is bonded initially with one center and then transits to the field of the second center, and one of these centers — potential wells for electrons — is a cluster, while the second one is located on the substrate. In this case, process (5.1) is described by the following scheme [42, 190]:

$$S - \mathrm{Au}_n^- \downarrow + \mathrm{CO} \to S^- - \mathrm{Au}_n \uparrow \cdot \mathrm{CO}\,, \tag{5.8}$$

where the S is a substrate, the arrow indicates the configuration state, and the point corresponds to a bound state. Note that according to measurements and on the basis of DFT-calculations [191, 192], the basic configuration state of a negatively charged gold cluster containing 12 atoms is a flat structure, whereas such a cluster consisting of 13 and 14 atoms has a spatial configuration of atoms. This shows that the configuration transition in this case proceeds simultaneously with charge transfer.

Thus, the oxidation process for CO molecules with gold clusters consisting of 10 atoms as a catalyst and a suitable substrate is a complex process. Figure 18 shows the configuration of the $\mathrm{Au_{10}}$ cluster, located on the MgO substrate, which follows from DFT-calculations [193]. This structure allows the fundamental character of the process to be

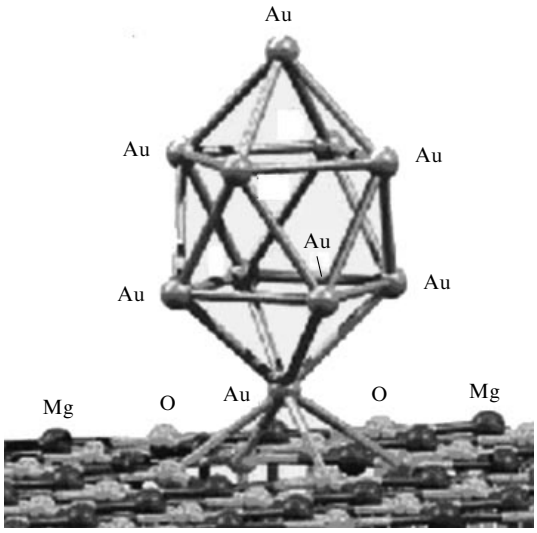

Figure 18. Structure evaluated on the basis of the density functional theory (DFT) for an MgO semiconductor as a support with gold clusters consisting of 10 atoms which are attached to the support surface [193]. A defect on the MgO surface is formed by the removal of one oxygen atom, and the lower atom of the gold cluster fastens to this defect. In the course of the chemical reaction with oxidation of the CO molecule, the gold cluster can change its configuration.

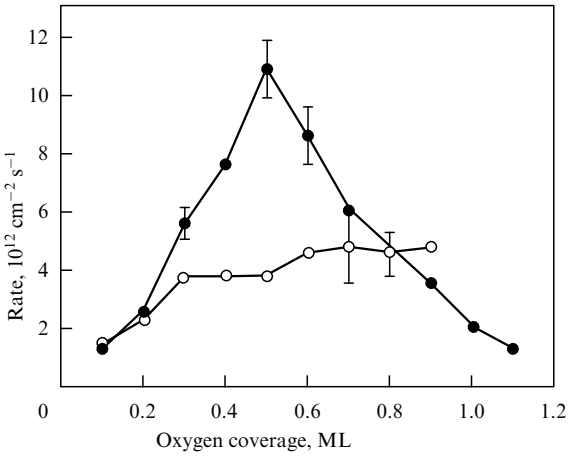

Figure 19. Dependence of the rate of formation of CO_2 molecules in process (5.7) on the degree of substrate covering by molecular oxygen at a temperature of 200 K (black dots) and 400 K (white dots) [195, 196]. ML means the number of molecular layers.

analyzed. According to experiments [81, 82, 84, 194] and the analysis, the capture of CO molecules occurs in a space at the boundary between the cluster and substrate. In addition, oxygen molecules of air may be further involved in the catalytic process (Fig. 19).

The catalyst under consideration provides oxidation of CO in air at room temperature, which is not available for other catalysts, and it is promising as an automotive filter. Nevertheless, the first application of this catalyst was for the removal of odors in Japanese toilets [81, 194, 197], where the main source is trimethylamine. Its decomposition upon using the catalyst under consideration leads to the formation of N_2 and CO_2 molecules, whereas decomposition of trimethylamine with palladium and platinum as the catalysts occurs at higher temperatures, and the product of this process is N_2O. The basis of this catalyst for the destruction of trimethylamine in this case is a zeolite powder containing $NiFe_2O_4$, to which gold clusters are attached, and an iron oxide powder Fe_2O_3 is the basis for the gold clusters. Next, this catalyst with gold clusters for CO oxidation in air is also suitable for the low temperature oxidation of hydrocarbons [198].

One area of use of this catalyst is in so-called green chemistry [199, 200]. In this case, products of chemical processes by oxidation in air are only water, carbon dioxide, and nitrogen. Nanocatalysis with gold clusters aims at oxidation processes and is useful for such processes [201]. In particular, this catalysis may be used to produce gluconic acid [202], acetic acid [186], and propylene oxide [203]. The nanocatalysis with gold clusters can provide high activity and selectivity of a chemical process. Within the framework of green chemistry, this catalyst can also be used for the decomposition of atmospheric ozone.

The system under consideration, consisting of a metal oxide surface and gold clusters fastened to it, may be used not only as a catalyst, but also in other processes. This system can be a sensor for CO detection [204], and also may be used to control the CO emission from car engines and for air purification [205]. It can be a basis for batteries and fuel cells using methane [206]. The chemical energy of the fuel cell is converted into electrical energy. In the hydrogen-oxygen fuel cell, hydrogen and oxygen are injected into the combustion chamber in the correct proportions and are converted into water vapor in the catalytic chemical process, with platinum as a catalyst. However, the addition of gold clusters to the platinum catalyst surface delays catalyst pollution and increases the efficiency of this process [207, 208].

The main impetus for multilateral research on nanocatalysis with gold clusters is connected with the possibility of using it as a car filter, which would justify expenses on fundamental research on the catalytic process. Apparently, it does not occur, because products of this process are not removed and clog the catalyst. However, just these studies have led to principal advances in the study of nanostructures. The developed experimental methods with electron microscope measurements allowed individual atoms in the structure to be seen. Other methods may be added to this, which simultaneously give additional information. In particular, CO molecules are effective emitters due to vibrational transitions, and the absorption lines of CO-molecules adsorbed by gold clusters are characterized by energy transfers of 2112 and 2151 cm^{-1} [209, 210], which differ slightly from the corresponding lines of free CO-molecules or those to be bonded in chemical compounds. This gives information about the character of the process.

The density functional theory (DFT) is the basis of computer simulation and allows one to analyze the configurations of different atomic elements. An example of such a structure is shown in Fig. 18. Note that the potential of the density functional theory follow first and foremost from the variational principle, which is intended only for the ground electron state of the system. This and a low accuracy in determining the electron energy does not allow comparing different configurations with respect to their electron energy. However, this method gives the capability to determine accurately the length of bonds for a certain configuration of atoms and, accordingly, to construct different configurations of the system. Therefore, one can construct suitable structures of atoms, as given in Fig. 18, but it is difficult to select the optimal structure. In addition, finally, the catalytic process is

of interest, and this process leads to the transition between structures and is characterized by the barrier height for this transition. Therefore, determination of the structure of this system, which consists of a substrate with fastened gold clusters and attached CO molecules, is only part of the problem.

The peculiarity of the structure under consideration, where a cluster is bonded with the crystal lattice of a semiconductor, is the requirement that the lattice not be distorted under the action of a fastened cluster, i.e., the distance between atoms in the cluster and lattice are close. In particular, if a gold cluster with the face-centered cubic structure is fastened to the surface of crystalline magnesium oxide MgO, the preferable structure of its surface is Au(100)/MgO(100), since the the crystal lattice constants for macroscopic gold, 4.08 Å, and for magnesium oxide 4.20 Å, are close, so that these compounds can be combined with a small distortion of the gold crystal lattice. Therefore, an Au_{10} cluster with the face-centered cubic structure may be used as the model structure for the nanocatalysis under consideration [84]. Nevertheless, the structure of gold atoms given in Fig. 18 and located above the MgO crystal lattice [193] has another atomic configuration. Evidently, this structure is excited with respect to the catalyst under consideration, and information about the static structure allows us to describe only partially the catalytic chemical process.

Note that processes involving CO and O_2 molecules with a nanocluster may occur in the same manner on a macroscopic gold surface with the terrace structure [84, 196, 211], as well as on the surface of free gold clusters [212, 213]. Nevertheless, process (5.7) proceeds more effectively if the gold cluster is fastened to the substrate, which is a metal oxide [188, 214] with a suitable distance between its atoms, so that attached atoms are located at the periphery of the gold cluster and at the cluster–substrate boundary [81, 194]. In this case, the bond lengths in the cluster vary slightly depending on the surface structure of the metal oxide [186, 215–218]. The character of subsequent attachments of reacting molecules to the cluster depends on the cluster structure, and it is usually assumed that the gold–substrate contact relates to the direction Au(111) of the gold surface [219–221], as shown in Fig. 2a.

The complexity of the process of catalytic CO oxidation with small gold clusters fastened to the substrate also follows from the dependence of the chemical process rate on the chemical composition and substrate structure. The simplest version of the substrate is the MgO crystal surface {111}; iron oxide α-Fe_2O_3, titanium oxide TiO_2, and cerium oxide CeO_2 are suitable for this goal. These oxides may be in the form of a macroscopic surface, micron-sized particles, or thin films, and the above list comprises all the materials that can serve as substrates for small gold clusters, as other compounds do not provide appreciable catalytic effect.

All these compounds contain oxygen, which can participate in the chemical process. In addition, these support materials are semiconductors, and their chemical bond with gold clusters can lead to cluster charging, which is of importance for the chemical process [84, 222–225]. It is believed that the cluster charge changes the character of its interaction with molecules. Structures of gold clusters containing 10 atoms are shown in Fig. 2, and the total cluster charge is $-0.88e$ and $-2.19e$ for the face-centered cubic cluster structure according to the calculations [225] and is equal to $-1.06e$ if the cluster consists of two antiprisms (Fig. 2b).

One can expect that the presence of gold in this catalyst makes it expensive. In fact, as will be shown later, the catalyst price is determined by other factors. Indeed, let us assume gold clusters on a catalytic surface to consist of 10 atoms, in accordance with [81, 185–187], but the basis of the Au_{10} cluster is the face-centered cubic lattice, as shown in Fig. 2a, i.e., containing 7 atoms in the lower layer and 3 atoms in the upper layer. In addition, we assume that the clusters occupy 1% of the substrate surface. From this, we have the surface density of gold atoms on a substrate being approximately $N_{Au} = 8 \times 10^{14}$ cm^{-2} [189], if the gold atoms form a surface layer. This gives for the gold mass per unit substrate area $M_{Au} = 10/7 \times 0.01 M N_{Au} = 4 \times 10^{-9}$ g cm^{-2}, where M is the gold atom mass. Being guided by the market value of gold, at 1,300 dollars per ounce, one can get a material specific price of this nanocatalyst below 0.3 cents per m^2. Thus, gold's contribution to the cost of nanocatalysts is relatively small and is determined by both the unique equipment to create, detect, and work with nano-objects, and qualified personnel to service these devices.

One characteristic of the catalytic process under consideration is the dependence of the reaction rate on the concentration of water vapor. This question was studied in detail in book [82], and the analysis reflects both the positive and the negative effect of water molecules on the rate of the process (5.7). Acceleration of the oxidation process by water vapor takes place both for gold and for the catalyst of other transition elements [226–230]. The mechanism of acceleration of process (5.7) under the action of water molecules [231] is associated with lowering the dissociation barrier for water molecules on the catalyst surface, which results in the formation of an oxygen atom O attached to the CO molecule. On the other hand, the formation of OH radicals or complexes containing these radicals leads to a reduction in the rate of the catalytic process [217, 232]. These facts also indicate the complexity of the process.

The analyzed catalytic process includes several successive stages proceeding through the formation of long-lived structures as intermediate stages of the process. However, the dynamic character of the catalytic process requires a certain flexibility, which appears under the term 'dynamic fluctuation' [222, 233] and leads to an efficient transition between the configuration states of the system at each intermediate stage. This means that effective transitions between configuration states of a system consisting of a catalyst and reacting molecule proceed mostly due to atom displacement. Since metal clusters can change the atom configuration more easily than the macroscopic surface can, in principle, they can be better catalysts than the macroscopic surface [234]. This potential is enhanced for metal clusters due to a larger number of configuration states with a low excitation energy [235–238], as well as to the possibility of the cluster charge changing in the course of this process.

Summing up the understanding of the catalytic process (5.7) and representing the process as a transition between the potential energy surfaces of the system [42, 239, 240], one can formulate a working scheme of this process. In the initial state, a free CO molecule interacts with a gold cluster attached to the macroscopic surface of a metal oxide, and they form a specific configuration, say, as shown in Fig. 18. The metal oxide surface is covered partially with oxygen and is not uniform, and it contains the centers (dislocations and

impurity atoms) at which positive and negative ions are formed. The configuration state formed in the attachment of CO molecules to a gold cluster corresponds to a simultaneous change in the structure of the cluster (for example, from a volume structure to a plane one) and a valence electron transition between the centers located in the cluster and substrate. In this regard, the opposite transition of bond breaking between the CO molecule and gold cluster with a substrate is accompanied by a change in the cluster structure and the transition of the valence electron. The subsequent process that leads to the final channel of the chemical reaction is responsible for bond formation between a CO molecule located on the substrate and an oxygen atom. This implies the release of a CO_2 molecule, i.e., bond breaking between this molecule and cluster. Apparently, this does not actually happen, i.e., the CO_2 molecule remains to be bonded with the cluster and substrate, which corresponds to catalyst contamination. This scheme demonstrates the complexity of the catalytic process. Confirmation of the complexity of this multistage catalyst process is that its rate is not described by the Arrhenius formula that is expressed through the activation energy of the chemical process characterizing the barrier height for this reaction.

It can be expected that the above nanocatalysis could be developed for relatively inexpensive car filters. Indeed, the annual production is more than 50 million automotive engines [241], where platinum, palladium, and rhodium are used as a catalyst to clean car motors at more than 200 tons per year [241]. One would expect that nanocatalysis based on gold would lead to big benefits. Unfortunately, this plan was not realized as was expected initially, apparently due to contamination of nanocatalysts. Nevertheless, development of gold-based nanocatalysis has led to essential changes in the field of physics and chemistry, which can not be overestimated. New methods are developed for the detection of nanostructures that allow one to see individual atoms. The DFT has allowed us to analyze complex systems containing various kinds of nanostructures. In addition, the nanocatalysis method using gold as a catalyst became the basis for some chemical processes, and these processes have occupied a certain place in modern chemistry. Therefore, the absence of success in catalytic CO oxidation in air does not reduce the value of nanocatalysis in science, which originated in connection with solving this problem.

As is seen, development of cluster applications has led to the creation of new materials, where small metal clusters are attached to the semiconductor surface at points of surface defects. Such a material may be used as a catalyst, in particular, in oxidation reactions of gas molecules at this stage of research. Metal clusters are suitable for this goal due to two properties. On the one hand, the binding energies of the atoms in them are sufficiently large, which makes it possible to conserve clusters in chemical processes. On the other hand, the configurational excitation energies for these clusters are relatively small, as demonstrated in Fig. 2.

Cluster interaction with a surface can lead to a change in its charge and, as follows from the analysis, the capture of a reacting molecule by a cluster takes place simultaneously with a change in the cluster configuration and its charge, which makes the process irreversible. Of importance for this process is the use of a metal oxide as a substrate material. Namely, an oxygen atom is taken from the substrate for the oxidation process, and its subsequent reduction results from attachment of an oxygen molecule. From this analysis, it follows that the properties of this material as a catalyst depend on both the type of metal and the number of cluster atoms, as well as on the substrate material.

5.2 Semiconductor conductometric nanosensors

There is a large set of methods to determine the concentration of atoms and molecules of a certain type in a buffer gas. Obviously, spectroscopic methods have a high sensitivity because of the relatively small width of the spectral absorption lines of atoms or molecules of a certain kind. Notably, the very high sensitivity results from the so-called two-step method of atom ionization [242, 243]. In this case, resonance radiation transfers the atoms in an excited state, and a laser beam of another wavelength, which is not able to ionize atoms in the ground state, causes ionization of excited atoms. It is clear that the detection of ions is characterized by a higher sensitivity than with neutral particles. The presented method allows one to detect up to one cesium atom located in a cubic centimeter of air at atmospheric pressure [242].

The high sensitivity of spectral methods is reflected in the optohalvanic method of atom detection in a weakly ionized gas, in particular, in a flame. An electric current flows through a gas under the action of an external electric field, i.e., this gas is a gas discharge plasma. It is irradiated with a beam of a tunable laser, and the laser wavelength is in resonance with the excitation of detected atoms. A certain portion of the excited atoms is ionized, which leads to an electric current spike of the circuit, and the amplitude of the electric current increase characterizes the number density of impurity atoms in the buffer gas. This method allows the detection of impurity atoms in the buffer gas, starting from concentrations of the order of 10^{-12} [244–246]. Of course, this method refers to impurity atoms with a low ionization potential, but the sensitivity of this method testifies to its potential.

Below, we concentrate on the method of measurement of impurity molecules in a buffer gas, where the presence of impurity molecules in the buffer gas and a change in their number density is detected due to the electric current change under the action of impurity molecules passing through the device or a change in the sensor's electrical resistance. In spite of the lower sensitivity than with spectroscopic methods, the sensors are spread because of the simplicity and compactness of these devices. The sensors currently used are called chemical nanosensors [247–249], because their effect is due to a chemical process on the conductor surface. Below, these sensors will be divided into semiconductor and metal, in accordance with the type of material which is used as a sensor conductor.

Semiconductor conductometric sensors are the most widely used, which have been investigated and used for several decades [250–254]. In particular, in the first decade of this century more than 2,000 published papers were devoted to this topic [249]. In this case, the electric current propagates through a semiconductor nanomaterial, and the electric current passed through a semiconductor changes under the influence of active molecules located in a surrounding buffer gas. This semiconductor can be in the form of single grains or nanowires [166, 167]. Oxides of some metals, such as ZnO, SnO_2, CuO, and WO_3, are typically used as the sensor conductor. An example of a semiconductor sensor is shown in Fig. 20, where the voltage is about 0.1 V and measured currents are 10 nA. This example shows the scale of values used in this method.

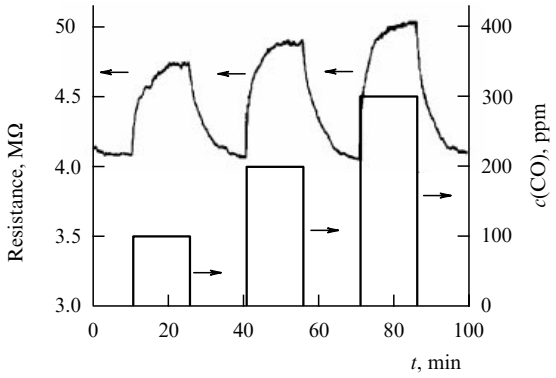

Figure 20. Dependence of the electrical resistance of a conductometric semiconductor sensor based on copper oxide CuO nanowires and palladium nanoclusters about 5 nm in diameter [166] in synthetic air at 350 °C and at a humidity of 50% with the addition of CO. The concentration of CO and its dependence on time is indicated. One ppm = 10^{-6} (parts per million).

There are two mechanisms of action of impurity molecules on the sensor resistance, as shown in Fig. 21. The first one (Fig. 21a) refers to a semiconductor composed of grains, where an active molecule acts on the space between neighboring grains. If chemical processes involving impurity molecules allow the destruction of the partition between neighboring grains, the sample resistance decreases. An opposite effect is possible where impurity molecules increase the energy barrier (the Schottky barrier) for a contact between neighboring grains, so that the sample resistance increases. Another mechanism given in Fig. 21b results from the surface charge appearance under the action of active molecules. By the way, in order to clean the conductor surface of attached molecules, which change the surface charge, metal nanoparticles are often added to the semiconductor to take the surface charge away.

One of the sensor important parameters is its sensitivity S, which is the ratio of the sensor resistance R_a in a gas with appropriate impurities to the resistance R_g of the sensor located in a test gas. It is taken into account that a resistance change results from the chemical reaction involving active molecules, and this changes the surface properties of the conductor and its conductivity near the surface. In the case of the activation character of the chemical process, its sensitivity with respect to a given gas depends on the gas temperature. An example of this is given in Fig. 22, and just the temperature dependence of the sensitivity allows us to determine the kind of impurity molecules. Therefore, semiconductor sensors include a heater that provides a measure of the sensor sensitivity in a certain temperature range, and the kind of impurity molecules is ascertained from this. As a result, semiconductor sensors allow determining with the appropriate accuracy the kind of impurity molecules and their concentration at values above 1 ppm.

The action of a conductometric semiconductor sensor in detecting active molecules in a buffer gas is based on measuring the semiconductor resistance. A change in the semiconductor resistance under the influence of interacting molecules greatly depends on the temperature. The action of impurity molecules on sensor resistance can be determined either by the attachment of detected molecules to the semiconductor surface with the formation chemical bonds with the surface or by chemical reactions involving these

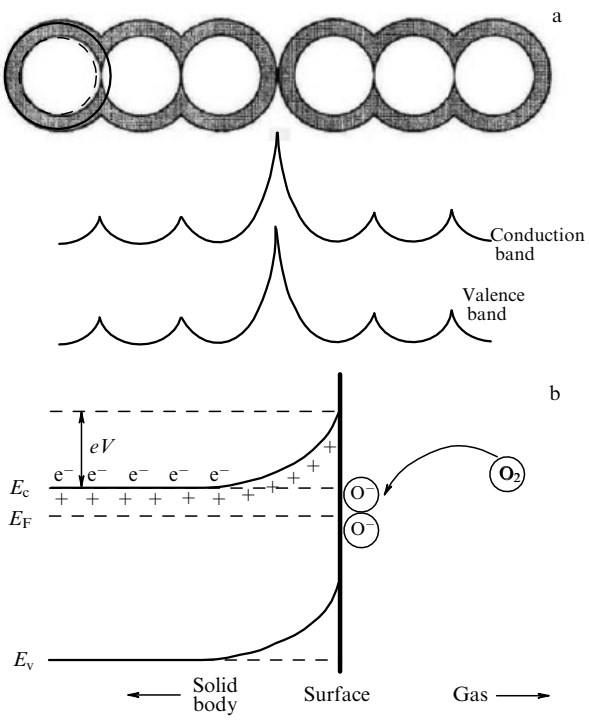

Figure 21. Mechanisms of influence of active molecules located in a buffer gas on the sensor conductor. (a) Active molecules change the partition separating semiconductor grains [255]; (b) change in the charge distribution near the semiconductor surface as a result of the attachment of oxygen molecules [256, 257]. Attaching to the semiconductor surface, oxygen molecules are converted into negative ions that changes the spatial charge distribution near the surface.

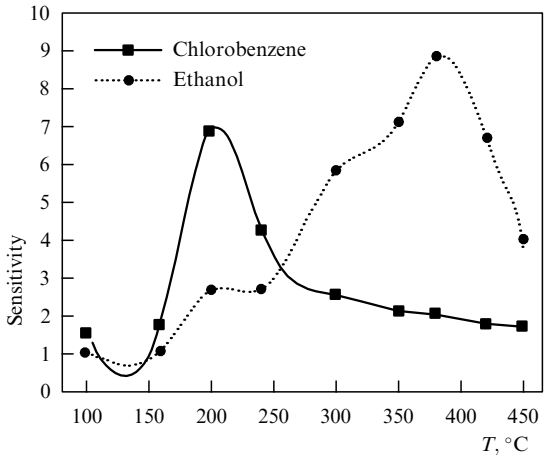

Figure 22. Temperature dependence of the sensitivity for a sensor based on porous ZnO in a surrounding buffer gas with chlorobenzene and ethanol at a concentration of 100 ppm [257, 258].

molecules. As a result, the character of energy bands changes near the semiconductor surface, which is reflected in its resistance. The temperature dependence of the semiconductor resistance characterizes the kind of attaching molecules. As a rule, a certain chemical composition of the semiconductor is used for each type of detected molecules (for example, [255, 259–261]).

Note that this method is used to measure concentrations of molecules in a buffer gas above $\sim 10^{-6}$. In addition, if detected molecules react chemically with the semiconductor

surface, the latter is clogged, i.e., the sensitivity decreases as the surface is covered with products of the chemical reaction. This is an irreversible process, i.e., surface cleaning is required at a certain stage of surface coverage.

5.3 Sensor based on metallic nanostructures

A sensor based on metal nanostructures may be considered the limiting case of a semiconductor sensor, where active molecules interact in the strongest manner with the conductor surface. In this case, there is Coulomb interaction of a negative ion, which is formed from an active molecule by attachment of a metal electron to it, and a positively charged hole, which is formed inside the metal. The strong interaction provides a higher sensitivity (by roughly three orders of magnitude) for metal nanosensors than for semiconductor ones. However, since this Coulomb interaction in metal nanosensors takes place for different types of active molecules, these sensors are not selective. Next, since the measurements are carried out in this case at lower molecule concentrations, the relative lifetime of the device in this case is much higher than that of the semiconductor conductometric sensor. In the case of a metal conductor, its cleaning may be fulfilled by using the flow of a gas discharge plasma, and the subsequent chromatographic analysis of products [262] allows one to determine the kind of attached active molecules or the distribution of these molecules over their types.

In Section 4.3, we consider the mechanism of sensor operation with metal nanostructures as a conductor (Fig. 16). This mechanism consists of the formation of a positively charged hole inside a metal under the action of a negative ion formed from an active molecule on the metal surface. This couple of charged particles acts on a valence electron, causing an increase in conductor resistance. From this, it follows that a nanometer transverse conductor size is optimal and the conductor of this sensor exists in the form of a metal nanostructure. Therefore, an analysis of the conductometric sensor lies in comparing the parameters of various metal nanostructures.

The main problem with this is the lack of sufficient information about electrical properties of metallic nanostructures. Therefore, we have to restrict ourselves to rough estimates of the resistance of a percolation cluster and of a system of interwoven nanofibers, and in the case of fractal fibers even estimates of these parameters are absent. Above (Section 2.3 and Figs 4, 5), some photographs are given for each nanostructure under consideration, which allows one to understand their general features and differences. The percolation cluster consists of grain-nanoclusters, whereas fractal fibers contain as their elements fractal aggregates of smaller sizes, and a fractal fiber itself has a small transversal dimension compared to the longitudinal one. The nanostructure resulting from superfluid helium is a system of interwoven metal nanowires and, apparently, this is the most convenient metal nanostructure for a conductor sensor.

The percolation cluster consisting of metal grains and used as a conductor of the conductometric sensor is a two-dimensional system and covers the tube surface through which a buffer gas with detected active molecules passes. Next, let us consider the fractal fiber, a three-dimensional system located inside the tube. Figure 5 contains a fragment of the fractal fiber, which gives an understanding of its structure. The fractal fiber is formed as a result of joining fractal aggregates under the action of interactions of dipole moments of fractal aggregates induced by an external electric field. In turn, the fractal aggregates [72] are isotropic fractal structures whose size does not exceed 1 μm and which are composed of metal nanoclusters with a typical size of about 10 nm. However, there is in this case also a general problem of restricted efficiency of fractal systems as elements of the sensor conductor, because a certain part of the structure remains at the periphery of the conductive channel and does not contribute to the resistance of this metal nanostructure as a conductor. Therefore, active molecules attached to this part of the nanostructure do not affect its electrical parameters.

A fractal fiber is an anisotropic fractal structure, and its anisotropy is created under the action of an electric field, beginning from sizes of the order of 0.1 μm, at which an electric field affects the character of structure growth (for example, [96]). Problems using this structure as a sensor conductor are connected with the fact that special experimental studies are required to determine the electrical resistance of the structure, and on the basis of this one can understand the advisability of using the fractal fiber as a sensor conductor.

Evidently, the most convenient fractal structure for a sensor conductor as of now is a bunch of metal nanofibers obtained in the process of evaporation and growth of metal nanofibers in superfluid helium [85–87]. The character of this process is described in Section 2.4 and uses the fact that superfluid helium repulses impurity atoms and particles outside it. As a result, evaporated metal atoms and metal nanoclusters formed from them are subsequently located in a space which is separated from the main volume of superfluid helium. The boundary of separation is conserved if metal particles are located inside the vortex. In this case, the kinetics of transformation processes of evaporated metal into nanoclusters are similar to those occurring in the nucleation of atomic metal vapor in a buffer gas (for example, [96]). Namely, atoms join into small metal cluster-drops, and further, in turn, small liquid clusters join with clusters of larger sizes, as long as they do not become solid.

The difference compared to the kinetics of cluster growth in a buffer gas at those stages of condensation of the metal vapor follows from the high thermal conductivity of liquid helium, and this leads to the formation of solid metal clusters at smaller sizes. The main difference in the kinetics of growth process takes place at the next stage, when solid clusters join into some structure in regions of their contact. As a result of joining solid clusters in a buffer gas, fractal aggregates are formed [72], i.e., structures where neighboring clusters are in random directions with respect to a given one. All solid clusters are located in one line in superfluid helium and form a chain of solid clusters at the first stage of the process.

Of course, the vortex length is restricted, and the observed length is estimated as $d \sim 100$ nm. Thereby the vortex-restricted channel with metal clusters generates an anisotropy of the formed metal structure. In the case of cluster associations in a buffer gas, on average, an isotropic fractal structure is formed at this stage of the process, i.e., fractal aggregates [72]. When a growing metal fiber reaches some length in the course of growth in superfluid helium, a vortex comes off from the metal surface, and then the vortex with a chain metal cluster inside it makes a diffusive motion in the superfluid helium. If its trajectory intersects with that of another vortex containing a chain metal cluster, these chains are bonded in the contact area. Accordingly, subsequent growth leads to the formation of fractal structures, whose element is a nanofiber about 100 nm in length and radius is a

few nanometers. This structure may be attached to walls or to other elements of a fixed structure, so that after helium removal, this system exists stably inside a buffer gas, as with other fractal structures discussed above.

The above description of the formation of the above metal nanostructure is entirely based on experimental data. In the following, the parameters of this structure were analyzed in more detail for catalytic applications [97–99]. In the author's opinion, only the metal property is used due to a large specific surface area, which is of the same order of magnitude as for other nanostructures. In addition, the experience with nanocatalysis for CO oxidation when using bonded gold clusters shows [42, 82, 183] that the substrate to which gold clusters fasten is of importance for this process. The metal cluster can be found in various configurations, between which a transition occurs in the catalytic process.

The significant advantage of the metal structure obtained from superfluid helium is a large length of metal nanowires compared to the radius of a nanocluster as elements of other nanostructures. This provides a smaller number of metal nanoclusters as a conductive channel and, accordingly, a higher efficiency of the metal structure for the main process. In particular, this means that in formulas (4.15), (4.16) a nanowire length that is of the order of $d \sim 100$ nm is used as the structural element, rather than a cluster radius of the order of a few nanometers.

In addition to this, we note that this structure consisting of interwoven metal nanowires is studied in more detail than an individual fractal fiber. A method has been worked out for conversion of a three-dimensional fractal structure obtained as a result of helium removal in a two-dimensional structure by its attachment to a dielectric located on the chamber walls. Although two-dimensional structures located on the walls of the sensor tube are more stable in the course of propagation of a buffer gas flow with active molecules through the tube filled by a fractal structure, we will be guided by the three-dimensional system consisting of interwoven metal nanowires.

One can add that the resistance of this structure has been measured, showing the possibility of using it as a sensor conductor. According to experimental data, a single nanowire has a resistance of 300 kΩ at a radius of 4 nm and a length of 100 nm for an elementary platinum nanowire if the total length of 1.6 mm corresponds to an experimental distance between electrodes. Let us compare this with the above formulas. According to formula (4.13), the effective conductor length L_{eff}, i.e., the total length of the conductor segments, consisting of a single fiber, for a given conductor resistance R is given by

$$L_{\text{eff}} = \frac{\pi r^2 R}{\rho_0} . \tag{5.9}$$

Under the above values of parameters, this formula gives $L_{\text{eff}} = 0.13$ mm (the specific resistance of platinum is $\rho_0 = 1.1 \times 10^{-5}$ Ω cm [109]). Formula (4.16), where we use this fiber length instead of its radius as a nanostructure element, gives for the total length of the conductive channel composed of individual fibers $L' = 0.17$ mm. Of course, a strong coincidence of results is apparent, since the estimates made are valid to a factor of 2–3. Nevertheless, the coincidence of the results demonstrates the correctness of the analysis. In addition, the above operations prove that single channels that determine the resistance of the conductive channel are a small part of the conductive channel length.

We consider a conductometric sensor with metallic nanostructures as a conductor in accordance with the scheme shown in Fig. 15, where the nanostructure is located in a tube or on its walls, and a test gas flows through the tube. Let us ascertain the character of the buffer gas flow with active molecules through the tube. We assume that a nanostructure is located on the tube walls, and attachment of active molecules to the metal walls leads to an increase in system resistance. Under these conditions, the mean free path of buffer gas molecules is large compared to the size of grains of the metal structure. Let us compare two typical times of the process, namely, the typical time of gas passage through the tube τ_{dr} and the time of attachment τ_{at} of active molecules to the inner tube surface. These times are determined by the formulas

$$\tau_{\text{dr}} = \frac{l}{u} , \quad \tau_{\text{at}} = \frac{b^2}{4D} , \tag{5.10}$$

where u is the flow velocity, which in this case is of the order of the sound speed, D is the diffusion coefficient of the active molecules in a buffer gas, being $D = 0.18$ cm^2 s^{-1} [263] for air molecules in air under normal conditions. For simplicity, we assume in formula (5.10) that every collision of an active molecule with a metal surface leads to molecule attachment to the surface. For definiteness, we are guided by the following parameters of the process as the tube length (the distance between the metal rings) $l = 1$ cm and the tube radius $b = 4$ mm (the initial width of the plate is about 2.5 cm). From formula (5.10), the drift time is $\tau_{\text{dr}} \sim 30$ μs under the above conditions. Formula (5.10) refers to the diffusion regime of propagation of active molecules in a buffer gas, so that the mean free path of active molecules in a buffer gas λ is small compared to the tube radius b ($\lambda \ll b$). This occurs if the air pressure is $p \gg 0.02$ Torr.

We consider the flow regime $\tau_{\text{dr}} \sim \tau_{\text{at}}$, where active molecules attach to the sensor walls. This corresponds to the buffer gas pressure $p \ll 0.1$ Torr, and since the rate of a buffer gas flow through a tube-orifice is of the order of the sound speed, from this it follows that the rate of gas flow does not exceed 80 sccm (unit of gas flow rate sccm — standard cubic centimeter of a gas per minute) or $\sim 4 \times 10^{19}$ s^{-1} for the molecule intensity. Taking the concentration of active molecules in air to be around 1 ppb (part per billion) $= 10^{-9}$, we have from this for the rate of attachment of active molecules to a metal surface $i \sim 4 \times 10^{10}$ s^{-1}. From this, it follows for a time τ_{min} through which a sensor electric current decreases by a measurable value as a result of attachment of active molecules to the surface sensor that

$$\tau_{\text{min}} = \frac{S n_{\text{cr}}}{i} , \tag{5.11}$$

where n_{cr} is the surface density of attached molecules, $S = 2\pi bl$ is the area of the sensor inner surface, and the minimum measurable surface density of active molecules n_{min} at measured values of the electric current is determined by formula (4.24). A typical time of measurement of this value τ_{min}, as follows from formula (5.11), is given in Table 8.

We now consider the case of a spatial nanostructure located inside the sensor-tube, taking into account that the mean free path λ of active molecules in a buffer gas is large compared with the fiber radius r of the fractal structure. Then, the collision cross section of an active molecule with a segment of a fiber radius r and length d is $2dr\cos\theta$, where θ

Table 8. Parameters of change of the nanostructure resistance inside the tube ($l = 1$ cm, $b = 0.4$ cm) with the parameters of platinum nanostructures ($d = 200$ nm, $S = 3.2$ cm^2).

Parameter \ Metal	Fe	Cu	Ag	Au
n_{cr}, 10^6 cm^{-2}	23	2.3	1.5	6.9
τ_{cr}, ms	1.5	0.11	0.10	0.44
τ_{max}, days	1.7	0.17	0.11	0.51
τ_{min}, ms	6	0.2	0.2	1

is the angle between the direction of movement of an active molecule and a fiber axis. Averaging over the angle, for the cross section of the active molecule with an element of the collision thread we obtain $\sigma = rd = s/(2\pi)$, where s is the surface area of a segment. Assuming, as before, that every collision of active molecules with the nanostructure surface leads to its sticking to the surface, we find that the rate of attachment of active molecules v to the nanostructure surface is given by

$$v = \frac{Sv_T}{2\pi V}, \tag{5.12}$$

where v_T is the thermal velocity of an active molecule, S is the total surface area of a nanostructure located inside the tube, and V is the volume inside the tube. Since a buffer gas flow propagates through a tube with the sound speed that is of the order of the thermal velocity, one can estimate from this the surface area that ensures attachment of active molecules to the nanostructure after passing a buffer gas through the tube,

$$S = \frac{2\pi V}{l}, \tag{5.13}$$

where l is the tube length. In particular, considering tube parameters ($l = 1$ cm, $V = 0.5$ cm^3) we have $S = 3.2$ cm^2, which is significantly lower than the surface area of the palladium nanostructure $S = 200$ cm^2, prepared experimentally [98] in about 10 min. This confirms the reality of preparation of the sensor conductor in the form of the nanostructures under consideration.

Being guided by optimal parameters for the attachment of active molecules to a nanostructure, we estimate below the sensor parameters. A typical sticking time of an active molecule to a nanostructure for the conditions under consideration is about $\tau \sim 1/v \sim 10^{-3}$ s. In determining the electric parameters of the nanostructure, we are guided by experimental data for platinum, which will also be used for other metals. Identifying the structure of interwoven fibers as a fractal structure with the fractal dimension $D = 1.74$ [264] and assuming, as before, that the main contribution to the structure resistance follows from single nanowires, we obtain the structure resistance $R = 1.2$ MΩ if the distance between electrodes is $l = 1$ cm. Then, the number n of elementary segments of length $d = 200$ nm in a conductive channel is

$$n = \left(\frac{l}{d}\right)^D. \tag{5.14}$$

From this, we have for the number of elementary segments in the nanostructure, which relate to a single conductive channel, $n = 1.5 \times 10^8$, while its surface area is $s = 7.5 \times 10^{-3}$ cm^2. Above, we have determined the optimal surface area of a nanostructure $S = 3.2$ cm^2, which ensures attachment of active molecules to the nanostructure if a buffer gas flow with active molecules passes through it. This gives for the number of single channels $S/s = 420$, and since they are connected in parallel, the resistance of the nanostructure is $R = 3.2$ kΩ. For the electric voltage used between the electrodes $U = 1$ V, this corresponds to the current strength through the nanostructure $I = 0.35$ mA.

The above data relate to a nanostructure which is free from attached molecules. We now determine the sensor sensitivity with the conductor in the form of a nanostructure, assuming that the limit of measurement corresponds to the relative change in the current strength $\Delta I_{min}/I = 10^{-6}$, in accordance with formula (4.25). From this, it follows that the minimum measurable change in the current strength $\Delta I_{min} \approx 0.3$ nA. Let us determine the parameters of attachment of active molecules to the nanostructure under consideration. For definiteness, let us take a buffer gas pressure of 1 atm and concentration of 1 ppb of active molecules, which corresponds to the intensity of the buffer gas flow of about 200 sccm. On the basis of formulas (4.23), (4.24), and (4.26), we obtain in this case for the density change in active molecules n_{cr} attached to the nanostructure, which is fixed as a result of the change of the nanostructure resistance due to attachment of active molecules in accordance with formula (4.24). Table 8 contains the limiting value n_{cr}, the surface density change for active molecules at the above parameters of the platinum nanostructure. In addition, Table 8 contains the typical time τ_{cr} which is responsible for the change to the surface density of active molecules in accordance with the formula

$$\tau_{cr} = \frac{n_{cr}S}{J_{ac}}, \tag{5.15}$$

where $J_{ac} = 5 \times 10^{11}$ s^{-1} is the flux of active molecules passing through the sensor, together with a buffer gas. In addition, Table 8 contains the saturation time τ_{max} for a nanostructure, which corresponds to the assumption that the process of nanostructure filling with active molecules occurs if the resistance increases by 10%, i.e., the parameter ξ is determined by formula (4.23), and is $\xi = 0.1$.

The sensor is a device which transforms the attachment of active molecules to the conductor surface in an electric signal [254]. The above estimates allow one to compare parameters of semiconductor and metal sensors. Since a change in the sensor conductivity is created by a small region of nanometer sizes near the surface, the requirement for the sensor is identical in both cases. In the case of a metal sensor, the influence of active molecules on the sensor is stronger, because the molecule is converted into a negative ion and acts on the metal surface through the ion Coulomb field. Therefore, the sensitivity of a sensor with a metal conductor is much stronger than that for the semiconductor sensor and allows one to detect active molecules with concentrations of active molecules, measured in ppb. On the other hand, the formation of negative ions provides the maximum influence of active molecules on the conductor, and hence selectivity in this case is completely absent.

In operation, the conductor surface of the sensor is covered with molecules attached to it. Table 8 contains values of time τ_{max} under typical parameters of this process. In the case of a semiconductor sensor, these molecules can be removed by an increase in temperature. The sensor with a metal conductor has no selectivity, which is inherent in the nature of this device. In addition, the process of attachment of

active molecules to the metal nanostructure is a nonequilibrium one. Indeed, the binding energy of an active molecule with the metal surface is ~ 1 eV, and therefore when the process is over, these molecules remain on the metal surface at room temperature.

In order to prepare the sensor for further measurements, it is necessary to clean the surface of the conductor of attached molecules. It is convenient to use for this goal a capillary discharge (for example, [265–267]), which, on the one hand, generates a narrow plasma flux in a pulse regime and, on the other hand, does not destroy the metal nanostructure, but tears away active molecules. This follows from a high electron energy and a low gaseous temperature that does not allow heating the buffer gas detaching active molecules from the metal surface. In particular, in the case of the above system of interwoven metal nanowires as a sensor conductor, the total electron energy for release of active molecules is about 5 μJ. If the energy is used to heat air located inside a sensor tube under normal conditions ($T = 273$ K, $p = 1$ atm), the air is heated by approximately 0.3 K. Under these conditions, a significant part of the energy of a nonequilibrium plasma located in the torch of a capillary discharge is contained in the electrons. Treatment of the metal surface by a plasma in this manner prepares the conductor for subsequent measurements.

A subsequent chromatographic analysis [262] of products of plasma cleaning allows one to determine the composition of active molecules and their chemical formulas; moreover, there is experience in such an analysis (for example, [268]). Note also that in the conductometric sensor with the metal nanostructure, a small part of the metal is used to originate the electric current. Thus, the difference between the semiconductor and metal sensors consists not only of the parameters of action of active molecules on the resistance of the sensor conductor, but also of the character of propagation of the electric current.

Summarizing the analysis of the conductometric sensor on the basis of metal nanostructures, we note that two factors are taken into account. First, the optimal resistance of the conductor in the course of measurements within the framework of the bridge scheme corresponds to its transverse submicron sizes, whereas a typical size of elements of the optimal structure is realized at nanometer sizes. From this, it follows that the conductor consists of a large number of nanometer fibers. Next, since active molecules must attach to these fibers in the course of the passing of a buffer gas flow with active molecules, the surface metal structure is not suitable for this purpose, i.e., fractal fibers and a bunch of metal nanowires formed in superfluid helium are optimal for this goal. These structures may be used not only as a sensor, but also to remove the active molecules from the flow, in particular, in hydrocarbon combustion processes.

By definition, the conductometric sensor is a device that allows one to determine the concentration of active molecules on the basis of the change in the resistance of the conductor which is the basis of this device. However, a conductometric semiconductor sensor and a sensor based on metal nanostructures are different devices. A conductometric semiconductor sensor has a certain selectivity and, in principle, allows the kind of active impurity to be determined. A conductometric sensor based on metallic nanostructures is characterized by the strongest action of active molecules on the metal conductivity, since these molecules form negative ions on the metal surface. Next, the surface of the conductometric semiconductor sensor is restored as a result of its temperature rise, whereas the sensor surface based on metallic structures is contaminated by the formation of compounds chemically bonded with the surface. Therefore, this sensor requires the replacement of the conductive element or may be restored by the action of a plasma torch. In addition, the sensitivity of the conductometric semiconductor sensor is significantly lower than that of sensors based on metal nanostructures. Thus, the conductometric semiconductor sensor and sensors based on metal nanostructures are fundamentally different devices.

One can expect that the problem of creating a conductometric sensor with optimal parameters is a technical one, although it is related to knowledge-based technology. However, the experience of this paper shows how fundamental and applied problems are intertwined in this case. The above analysis of using metal nanostructures as a sensor conductor allows one to give only rough estimates of the electrical parameters of these systems and processes with their participation; in the case of fractal fibers, even such estimations are impossible. Nevertheless, this analysis allows us to understand the possibilities of using metal sensors and to construct its optimal scheme. In particular, from this, it follows that two nanostructures, a fractal fiber and a bunch of interwoven nanowires, may be used as a sensor conductor. In turn, applied research aimed at creating a sensor with optimal parameters initiates the fundamental experimental studies that provide information about the electric properties of nanostructures, which is necessary for a deeper analysis.

6. Conclusions

At the present stage of study of metal clusters, the focus has shifted to nanostructures, i.e., systems of bound metal nanoclusters or nanowires. These systems, as physical objects, may be divided into two classes: surface, where the nanostructure exists on the surface, and three-dimensional, with the location of nanostructures in a certain volume (as fractal fibers). The nanostructure is fastened to the surface by its endings. In turn, surface nanostructures may be divided into two groups, where fastened nanoparticles are located on the surface, clusters or fibers do not interact with each other, or chemical bonds are established between nearest neighbors. In the last case, solid clusters form a net on the surface. A spatial three-dimensional nanostructure may be modelled by a web.

Effectively, nanostructures are a new material, and surface nanostructures may refer to a certain class of films. Therefore, some applications of nanostructures are similar to those of films. However, the main interest in nanostructures is that they consist of nanoparticles, which determine some properties of nanostructures. These properties make it possible to use them as a catalyst, as well as a sensor conductor. In this case, since the size of nanoparticles as elements of a nanostructure significantly exceeds atomic sizes, the properties of metals are manifested in nanostructures.

In connection with the problems under consideration, the following properties of metals are of interest. The first concerns the competition of structures for small clusters attached to the surface. In contrast to dielectric clusters, where the ground configuration state is separated from the first excited state by a relatively large energy gap at the magic number of atoms in a cluster, in the case of metal clusters, the excitation energy of the configurations is small if it is

compared with the binding energy of atoms in the cluster. Therefore, the transitions between configuration states of metal clusters proceed efficiently. Moreover, as the number of cluster atoms varies, the configuration of atoms in the ground state may change.

We note that the subject of our consideration is transition metals, in which s- and d-electron shells of valence electrons compete. These shells are transformed into s- and d-energy bands for valence electrons of macroscopic metals. Since the size of nanoclusters in the nanostructures significantly exceeds the typical atomic size, this property of macroscopic metals also relates to clusters. The transition between these energy bands of valence electrons is also typical for clusters and nanowires which form nanostructures.

It is of importance that some transition metals are easily oxidized in air or gases containing a small admixture of oxygen, and in applied problems nanostructures often border an air or gases containing oxygen. In this case, an oxide film is formed on the surface of macroscopic metals, which usually protects them from the penetration of oxygen deep into the metal. Since clusters and nanowires contain a restricted number of layers, the penetration of oxygen into the nanostructures is of special interest.

In conclusion, we note that nanostructures consisting of metal clusters or fibers are of practical interest. However, since nanostructures are simultaneously physical objects, it is necessary to study their properties, as well as the processes involving them. Therefore, the fundamental and applied studies of these objects are interwoven.

This paper was supported by a grant from Russian Science Foundation (grant 14-50-00124). The author thanks M Sowwan (Okinawa Institute of Science and Technology) for valuable discussions.

References

1. Echt O, Sattler K, Recknagel E *Phys. Rev. Lett.* **47** 1121 (1981)
2. Haberland H (Ed.) *Clusters of Atoms and Molecules*: *Theory, Experiment, and Clusters of Atoms* (Berlin: Springer-Verlag, 1994); Haberland H (Ed.) *Clusters of Atoms and Molecules II*: *Solvation and Chemistry of Free Clusters, and Embedded, Supported, and Compressed Clusters* (Berlin: Springer-Verlag, 1994)
3. Lakhno V D *Klastery v Fizike, Khimii i Biologii* (Clusters in Physics, Chemistry and Biology) (Moscow–Izhevsk: RKhD, 2001)
4. Suzdavev I P *Nanotekhnologiya*: *Fiziko-Khimiya Nanoklasterov, Nanostruktur i Nanomaterialov* (Nanotechnology: Physics and Chemistry of Nanoclusters, Nanostructures and Nanomaterials) (Moscow: KomKniga, 2006)
5. Echt O et al. *Ber. Bunsengesell. Phys. Chem.* **86** 860 (1982)
6. Ding A, Hesslich J *Chem. Phys. Lett.* **94** 54 (1983)
7. Harris I A, Kidwell R S, Northby J A *Phys. Rev. Lett.* **53** 2390 (1984)
8. Phillips J C *Chem. Rev.* **86** 619 (1986)
9. Harris I A et al. *Chem. Phys. Lett.* **130** 316 (1986)
10. Miehle W et al. *J. Chem. Phys.* **91** 5940 (1989)
11. Mackay A L *Acta Cryst.* **15** 916 (1962)
12. Arslan H, Güven M H *New J. Phys.* **7** 60 (2005)
13. Arslan H, Güven M H *Acta Phys. Slovac.* **56** 511 (2006)
14. Yildirim E K, Atis M, Guvenc Z B *Phys. Scr.* **75** 111 (2007)
15. Häberlen O D et al. *J. Chem. Phys.* **106** 5189 (1997)
16. Doye J P K, Wales D J *J. Chem. Soc. Faraday Trans.* **93** 4233 (1997)
17. Miller M A, Doye J P K, Wales D J *Phys. Rev. E* **60** 3701 (1999)
18. Wilson N T, Johnston R L *Eur. Phys. J. D* **12** 161 (2000)
19. Darby S et al. *J. Chem. Phys.* **116** 1536 (2002)
20. Wang J, Wang G, Zhao J *Phys. Rev. B* **66** 035418 (2002)
21. Smirnov B M *Plasma Processes and Plasma Kinetics* (Weinheim: Wiley-VCH, 2007)
22. Faraday M *Phil.Trans. R. Soc. Lond.* **147** 145 (1857)
23. Zsigmondy R *Lieb. Ann.* **301** 29 (1898)
24. Steubing W *Ann. Physik* **24** 1 (1907); *Ann. Physik* **26** 329 (1908)
25. Weitz D A, Oliveria M *Phys. Rev. Lett.* **52** 1433 (1984)
26. Weitz D A et al. *Phys. Rev. Lett.* **53** 1657 (1984)
27. Weitz D A et al. *Phys. Rev. Lett.* **54** 1416 (1985)
28. Keefer K D, Schaefer D W *Phys. Rev. Lett.* **56** 2376 (1986)
29. Wilcoxon J P, Martin J E, Schaefer D W *Phys. Rev. A* **39** 2675 (1989)
30. Weiser H B *Colloid Chemistry* (New York: J. Wiley and Sons, 1939)
31. Zheng J, Chen Z, Liu Z *Langmuir* **16** 9673 (2000)
32. Bell A T *Science* **299** 1688 (2003)
33. Xiao Y et al. *Science* **299** 1877 (2003)
34. Xiao L et al. *J. Chem. Phys.* **124** 114309 (2006)
35. Gu X et al. *Phys. Rev. B* **70** 205401 (2004)
36. Fa W, Dong J *J. Chem. Phys.* **124** 114310 (2006)
37. Fernández E M et al. *Phys. Rev. B* **70** 165403 (2004)
38. Johansson M P et al. *Phys. Rev. A* **77** 053202 (2008)
39. Smirnov B M *Principles of Statistical Physics* (Weinheim: Wiley-VCH, 2006)
40. Gilb S et al. *J. Chem. Phys.* **116** 4094 (2002)
41. Furche F et al. *J. Chem. Phys.* **117** 6982 (2002)
42. Berry R S, Smirnov B M *Phys. Rep.* **527** 205 (2013)
43. Ganteför G et al. *Faraday Discuss. Chem. Soc.* **88** 16 (1988)
44. Taylor K J et al. *J. Chem. Phys.* **96** 3319 (1992)
45. Edwards P P et al. *Phil. Trans. R. Soc. A* **356** 5 (1998)
46. Bardeen J *J. Appl. Phys.* **11** 88 (1940)
47. Ehrenreich H *Sci. Am.* **217** 194 (1967)
48. Mott N F *Metal-Insulator Transitions* (London: Taylor and Francis, 1974)
49. Mott N F *Metal-Insulator Transitions* (London: Taylor and Francis, 1990)
50. Hubbard J *Proc. R. Soc. A* **276** 238 (1963)
51. Hubbard J *Proc. R. Soc. A* **277** 237 (1964)
52. Hubbard J *Proc. R. Soc. A* **281** 401 (1964)
53. Chesnovsky O et al. *Chem. Phys. Lett.* **138** 119 (1987)
54. Busani R, Folkers M, Chesnovsky O *Phys. Rev. Lett.* **81** 3836 (1998)
55. Avnir D (Ed.) *The Fractal Approach to Heterogeneous Chemistry*: *Surfaces, Colloids, Polymers* (Chichester: Wiley, 1989)
56. Vicsek T *Fractal Growth Phenomena* (Singapore: World Scientific, 1989)
57. Smirnov B M *Fizika Fraktal'nykh Klasterov* (Physics of Fractal Clusters) (Moscow: Nauka, 1991)
58. Gouyet J-F *Physics and Fractal Structures* (New York: Springer, 1996)
59. Nakayama T, Yakubo K *Fractal Concepts in Condensed Matter Physics* (Berlin: Springer, 2003)
60. Mandelbrot B B *The Fractal Geometry of Nature* (San Francisco: W.H. Freeman, 1982)
61. Feder J *Fractals* (New York: Plenum Press, 1988)
62. Smirnov B M *Phys. Rep.* **188** 1 (1990)
63. Meakin P *Phys. Rev. A* **29** 997(R) (1984)
64. Jullien R, Kolb M, Botet R *J. Physique* **45** L211(1984)
65. Kolb M *Phys. Rev. Lett.* **53** 1653 (1984)
66. Botet R, Jullien R, Kolb M *Phys. Rev. A* **30** 2150(R) (1984)
67. Meakin P *J. Colloid Interface Sci.* **102** 491 (1984)
68. Kim S G, Brock J R *J. Colloid Interface Sci.* **116** 431 (1987)
69. Meakin P *Phys. Rev. Lett.* **51** 1119 (1983)
70. Wigner E, Seitz F *Phys. Rev.* **46** 509 (1934)
71. Wigner E *Phys. Rev.* **46** 1002 (1934)
72. Forrest S R, Witten T A (Jr.) *J. Phys. A* **12** L109 (1979)
73. Witten T A (Jr.), Sander L M *Phys. Rev. Lett.* **47** 1400 (1981)
74. Lushnikov A A, Negin A E, Pakhomov A V *Chem. Phys. Lett.* **175** 138 (1990)
75. Lushnikov A A, Pakhomov A V, Chernyaeva G A *Sov. Phys. Dokl.* **32** 45 (1987); *Dokl. Akad. Nauk SSSR* **292** 86 (1987)
76. Kolb M, Botet R, Jullien R *Phys. Rev. Lett.* **51** 1123 (1983)
77. Jullien R, Botet R *Aggregation and Fractal Aggregates* (Singapore: World Scientific, 1987)
78. Lushnikov A A et al. *Sov. Phys. Usp.* **34** 160 (1991); *Usp. Fiz. Nauk* **161** (2) 113 (1991)
79. Smirnov B M *Sov. Phys. Usp.* **34** 711 (1991); *Usp. Fiz. Nauk* **161** (8) 141 (1991)
80. Bond G C *Catalysis by Metals* (London: Academic Press, 1962)
81. Haruta M *Chem. Rec.* **3** 75 (2003)

82. Bond G C, Louis C, Thompson D T *Catalysis by Gold* (Singapore: World Scientific, 2006)
83. Kolasinski K W *Surface Science*: *Foundations of Catalysis and Nanoscience* (Chichester: Wiley, 2012)
84. Coquet R, Howard K L, Willock D J *Chem. Soc. Rev.* **37** 2046 (2008)
85. Gordon E B et al. *Low Temp. Phys.* **36** 590 (2010); *Fiz. Nizk. Temp.* **36** 740 (2010)
86. Gordon E B et al. *JETP* **112** 1061 (2011); *Zh. Eksp. Teor. Fiz.* **139** 1209 (2011)
87. Gordon E B et al. *Chem. Phys. Lett.* **519 – 520** 64 (2012)
88. Landau L D *J. Phys. USSR* **5** 71 (1941); *Zh. Eksp. Teor. Fiz.* **11** 592 (1941)
89. Lifshitz E M, Pitaevskii L P *Statistical Physics* Vol. 2 (Oxford: Pergamon Press, 1980); Translated from Russian: *Statisticheskaya Fizika* Vol. 2 (Moscow: Nauka, 1978)
90. Feynman R P *Statistical Mechanics* (Reading, Mass.: W.A. Benjamin, 1972); Translated into Russian: *Statisticheskaya Mekhanika* (Moscow: Mir, 1978)
91. Landau L D, Lifshitz E M *Fluid Mechanics* (Oxford: Pergamon Press, 1987); Translated from Russian: *Gidrodinamika* (Moscow: Nauka, 1988)
92. Williams G A, Packard R E *Phys. Rev. Lett.* **33** 280 (1974)
93. Berloff N G, Roberts P H *Phys. Rev. B* **63** 024510 (2000)
94. Gordon E B et al. *JETP Lett.* **85** 581 (2007); *JETP Lett.* **85** 710 (2007)
95. Gordon E B, Okuda Y *Low Temp. Phys.* **35** 209 (2009); *Fiz. Nizk. Temp.* **35** 278 (2009)
96. Smirnov B M *Nanoclusters and Microparticles in Gases and Vapors* (Berlin: De Gruyter, 2012)
97. Gordon E B et al. *J. Phys. Chem. Lett.* **5** 1072 (2014)
98. Gordon E B et al. *High Energy Chem.* **50** 292 (2016); *Khim. Vys. Energ.* **50** 305 (2016)
99. Gordon E B et al. *Theor. Eksp. Khim.* **52** 75 (2016)
100. Gordon E B et al. *Gold Bull.* **48** 119 (2015)
101. Becker E W, Bier K, Henkes W *Z. Phys.* **146** 333 (1956)
102. Henkes W *Z. Naturforsch. A* **16** 842 (1961)
103. Henkes W *Z. Naturforsch. A* **17** 786 (1962)
104. Smirnov B M *Phys. Usp.* **46** 589 (2003); *Usp. Fiz. Nauk* **173** 609 (2003)
105. Smirnov B M *Clusters and Small Particles in Gases and Plasmas* (New York: Springer, 1999)
106. Smirnov B M *Cluster Processes in Gases and Plasmas* (Wenheim: Wiley, 2010)
107. Vorob'ev V S *Phys. Usp.* **36** 1129 (1993); *Usp. Fiz. Nauk* **163** (12) 51 (1993)
108. Landau L D, Lifshitz E M *Electrodynamics of Continuous Media* (Oxford: Pergamon Press, 1984); Translated from Russian: *Elektrodinamika Sploshnykh Sred* (Moscow: Nauka, 1988)
109. Lide B K (Ed.) *Handbook of Chemistry and Physics* 86th ed. (London: CRC Press, 2003, 2004)
110. Landau L D, Lifshitz E M *Fluid Mechanics* (Oxford: Butterworth, 2000); Translated from Russian: *Gidrodinamika* (Moscow: Nauka, 1988)
111. Wien W *Ann. Physik* **58** 662 (1896)
112. Kask N E et al. *Quantum Electron.* **32** 437 (2002); *Kvantovaya Elektron.* **32** 437 (2002)
113. Kask N E, Michurina S V, Fedorov G M *Quantum Electron.* **33** 57 (2003); *Kvantovaya Elektron.* **33** 57 (2003)
114. Smirnov B M, in *Proc. of the 8th European Physics Conf. Trends in Physics* (Ed. F Pleiter) (Amsterdam: North-Holland, 1990) p. 84
115. Smirnov B M *Teplofiz. Vys. Temp.* **29** 185 (1991)
116. Anisimov S I et al. *Deistvie Izlucheniya Bol'shoi Moshchnosti na Metally* (Action of High-Power Radiation on Metals) (Moscow: Nauka, 1970)
117. Bronin S Ya, Polishchuk V P *Teplofiz. Vys. Temp.* **22** 550 (1984)
118. Brykin M V, Vorob'ev V S, Shelyukhaev B P *Teplofiz. Vys. Temp.* **25** 468 (1987)
119. Standa Catalog. Lasers and Laser Accessories, http://www.standa.lt/products/catalog/lasers_laser_accessories
120. Diode Pumped Solid State Air Cooled Picosecond Lasers, http://passatltd.com/dpss-picosecond-lasers
121. Penning F M *Physica* **3** 873 (1936)
122. Kay E *J. Appl. Phys.* **34** 760 (1963)
123. Gill W D, Kay E *Rev. Sci. Instrum.* **36** 277 (1965)
124. Wasa K, Hayakawa S *Rev. Sci. Instrum.* **40** 693 (1969)
125. Mullay J R *Res. Dev.* **22** (2) 40 (1971)
126. Shyjumon I, PhD Thesis (Greifswald: Greifswald Univ., 2005)
127. Kashtanov P V, Smirnov B M, Hippler R *Phys. Usp.* **50** 455 (2007); *Usp. Fiz. Nauk* **177** 473 (2007)
128. Child C D *Phys. Rev. Ser. I* **32** 492 (1911)
129. Langmuir I *Phys. Rev.* **2** 450 (1913)
130. Smirnov B M *Reference Data on Atomic Physics and Atomic Processes* (Heidelberg: Springer, 2008)
131. Holstein T *J. Phys. Chem.* **56** 832 (1952)
132. Haberland H et al. *Phys. Rev. Lett.* **69** 3212 (1992)
133. Haberland H et al. *J. Vac. Sci. Technol. A* **10** 3266 (1992)
134. Haberland H et al. *Mater. Sci. Eng. B* **19** 31 (1993)
135. Haberland H et al. *Z. Phys. D* **26** 8 (1993)
136. Haberland H et al. *J. Vac. Sci. Technol. A* **12** 2925 (1994)
137. Haberland H et al., in *Proc. of the 2nd Intern. Conf. on Beam Processing of Advanced Materials, Cleveland, OH, 30 October – 2 November 1995*
138. Haberland H et al. *Surf. Rev. Lett.* **03** 887 (1996)
139. Smirnov B M *Phys. Usp.* **37** 621 (1994); *Usp. Fiz. Nauk* **164** 665 (1994)
140. Smirnov B M, Strizhev A Ju *Phys. Scr.* **49** 615 (1994)
141. Smirnov B M *Phys. Usp.* **40** 1117 (1997); *Usp. Fiz. Nauk* **167** 1169 (1997)
142. Shyjumon I et al. *Thin Solid Films* **500** 41 (2006)
143. Kashtanov P V, Smirnov B M, Hippler R *Europhys. Lett.* **91** 63001 (2010)
144. Oxford Applied Research: Nanocluster Solutions, http://www.oaresearch.co.uk/oaresearch/brochures/nanocluster%20solutions.pdf
145. Klimov A et al., AIAA Papers 2011-1323 (Reston, VA: American Institute of Aeronautics and Astronautics, 2011)
146. Klimov A et al., AIAA Papers 2011-3285 (Reston, VA: American Institute of Aeronautics and Astronautics, 2011)
147. Kashtanov P V, Smirnov B M, Bityurin V A, Klimov A I *Europhys. Lett.* **96** 33002 (2011)
148. Smirnov B M *Europhys. Lett.* **97** 33001 (2012)
149. Smirnov B M *Proc. Int. Conf. "Nanoclusters Synthesis, Characterization and Potential Applications"* (Okinawa Institute of Science and Technology, 2016, p. 23)
150. Smirnov B M *Phys. Usp.* **54** 691 (2011); *Usp. Fiz. Nauk* **181** 713 (2011)
151. Smirnov B M *JETP* **121** 587 (2015); *Zh. Eksp. Teor. Fiz.* **148** 675 (2015)
152. Lifshitz E M, Pitaevskii L P *Physical Kinetics* (Oxford: Pergamon Press, 1981); Translated from Russian: *Fizicheskaya Kinetika* (Moscow: Nauka, 1988)
153. Dyer S A (Ed.) *Wiley Survey of Instrumentation and Measurement* (New York: Wiley, 2001)
154. Bhargava S C *Electric Measuring Instruments and Measurements* (London: CRC Press, 2012)
155. Sommerfeld A, Bethe H, in *Handbuch der Physik* Vol. 24, 2nd ed. (Berlin: Springer, 1933) p. 333
156. Ashcroft N W, Mermin N D *Solid State Physics* (New York: Holt, Rinehart and Winston, 1976)
157. Kittel Ch *Introduction to Solid State Physics* (New York: Wiley, 1986)
158. Smirnov B M *Phys. Usp.* **45** 1251 (2002); *Usp. Fiz. Nauk* **172** 1411 (2002)
159. Bhattacharyya S R et al. *JETP* **107** 1009 (2008); *Zh. Eksp. Teor. Fiz.* **134** 1181 (2008)
160. Bhattacharyya S R et al. *J. Phys. D* **42** 035306 (2009)
161. Feder J *Fractals* (New York: Plenum Press, 1988) p. 108
162. Stauffer D *Introduction to Percolation Theory* (London: Taylor and Francis, 1985)
163. Pike R, Stanley H E *J. Phys. A* **14** L169 (1981)
164. Jullien R, Kolb M *J. Phys. A* **17** L639 (1984)
165. Kim I-D, Rothschild A, Tuller H L *Acta Mater.* **61** 974 (2013)
166. Steinhauer S et al. *Nanotechnology* **26** 175502 (2015)
167. Steinhauer S et al. *ACS Sens.* **1** 503 (2016)
168. Smirnov B M *Negative Ions* (New York: McGrow-Hill, 1982) p. 28

169. Gates B C, Guczi L, Knözinger H (Eds) *Metal Clusters in Catalysis* (Amsterdam: Elsevier, 1986)
170. Gates B C *Chem. Rev.* **95** 511 (1995)
171. Henry C R *Appl. Surf. Sci.* **164** 252 (2000)
172. Alexander J W *Surgical Infections* **10** 289 (2009)
173. Liau S Y et al. *Lett. Appl. Microbiol.* **25** 279 (1997)
174. Gupta A, Silver S *Nature Biotechnol.* **16** 888 (1998)
175. Nomiya K et al. *J. Inorg. Biochem.* **98** 46 (2004)
176. Morones J R et al. *Nanotechnology* **16** 2346 (2005)
177. Nam G et al. *Nanomater. Nanotechnol.* **5** 23 (2015)
178. Lu Z et al. *J. Mater. Sci. Mater. Med.* **24** 1465 (2013)
179. Agnihotri S, Mukherji S, Mukherji S *RSC Adv.* **4** 3974 (2014)
180. Heiz U, Landman U (Eds) *Nanocatalysis* (Heidelberg: Springer, 2007)
181. Moshfegh A Z *J. Phys. D* **42** 233001 (2009)
182. Gellman A J, Shukla N *Nature Mater.* **8** 87 (2009)
183. Haruta M *Catal. Today* **36** 153 (1997)
184. Haruta M et al. *Chem. Lett.* **16** 405 (1987)
185. Bondzie V A, Parker S C, Campbell C T *Catal. Lett.* **63** 143 (1999)
186. Christensen C H et al. *Angew. Chem. Int. Ed.* **45** 4648 (2006)
187. Herzing A A et al. *Science* **321** 1331 (2008)
188. Haruta M et al. *J. Catal.* **115** 301 (1989)
189. Haruta M, Daté M *Appl. Catal. A* **222** 427 (2001)
190. Berry R S, Smirnov B M *Europhys. Lett.* **97** 63003 (2012)
191. Li J et al. *Science* **299** 864 (2003)
192. Liu Z-P et al. *Phys. Rev. Lett.* **91** 266102 (2003)
193. Molina L M, Hammer B *Phys. Rev. B* **69** 155424 (2004)
194. Haruta M *CATTECH* **6** 102 (2002)
195. Min B K et al. *J. Phys. Chem. B* **110** 19833 (2006)
196. Min B K, Friend C M *Chem. Rev.* **107** 2709 (2007)
197. Ueda A, Haruta M *Resources Environment* **28** 1035 (1992)
198. Tian N et al. *Science* **316** 732 (2007)
199. Hutchings G J *Gold Bull.* **37** 3 (2004)
200. Christensen C H, Nørskov J K *Science* **327** 278 (2010)
201. Corma A, Garcia H *Chem. Soc. Rev.* **37** 2096 (2008)
202. Biella S, Prati L, Rossi M *J. Catal.* **206** 242 (2002)
203. Sinha A K et al. *Topics Catal.* **29** 95 (2004)
204. Funazaki N et al. *Sensors Actuators B* **14** 536 (1993)
205. Corti C W, Holliday R J, Thompson D T *Topics Catal.* **44** 331 (2007)
206. Biswas P C et al. *J. Electroanalyt. Chem.* **381** 167 (1995)
207. Zhang J et al. *Science* **315** 220 (2007)
208. Winther-Jensen B et al. *Science* **321** 671 (2008)
209. Dekkers M A P, Lippits M J, Nieuwenhuys B E *Catal. Lett.* **56** 195 (1998)
210. Dekkers M A P, Lippits M J, Nieuwenhuys B E *Catal. Today* **54** 381 (1999)
211. Liu Z-P, Hu P, Alavi A *J. Am. Chem. Soc.* **124** 14770 (2002)
212. Salisbury B E, Wallace W T, Whetten R L *Chem. Phys.* **262** 131 (2000)
213. Wallace W T, Whetten R L *J. Phys. Chem. B* **104** 10964 (2000)
214. Haruta M *Catal. Surf. Jpn.* **1** 61 (1997)
215. Valdren M, Lai X, Goodman D W *Science* **281** 1647 (1998)
216. Wahlström E et al. *Phys. Rev. Lett.* **90** 026101 (2003)
217. Lopez N et al. *J. Catal.* **225** 86 (2004)
218. Chen M, Goodman D W *Acc. Chem. Res.* **39** 739 (2006)
219. Roberts J T, Capote A J, Madix R J *Surf. Sci.* **253** 13 (1991)
220. Chan A S Y, Deiner L J, Friend C M *J. Phys. Chem. B* **106** 13318 (2002)
221. Webb M J, Driver S M, King D A *J. Phys. Chem. B* **108** 1955 (2004)
222. Häkkinen H et al. *J. Phys. Chem. A* **107** 6168 (2003)
223. Sanchez A et al. *J. Phys. Chem. A* **103** 9573 (1999)
224. Yoon B et al. *Science* **307** 403 (2005)
225. Coquet R et al. *J. Mater. Chem.* **16** 1978 (2006)
226. Schaub R et al. *Phys. Rev. Lett.* **87** 266104 (2001)
227. Kung H H, Kung M C, Costello C K *J. Catal.* **216** 425 (2003)
228. Sanchez-Castillo M A et al. *Angew. Chem. Int. Ed.* **43** 1140 (2004)
229. Daté M et al. *Angew. Chem. Int. Ed.* **43** 2129 (2004)
230. Costello C K et al. *J. Phys. Chem. B* **108** 12529 (2004)
231. Liu L M et al. *J. Am. Chem. Soc.* **128** 4017 (2006)
232. Bongiorno A, Landman U *Phys. Rev. Lett.* **95** 106102 (2005)
233. Harding C et al. *J. Am. Chem. Soc.* **131** 538 (2009)
234. Moseler M, Häkkinen H, Landman U *Phys. Rev. Lett.* **89** 176103 (2002)
235. Koga K, Ikeshoji T, Sugarawa K *Phys. Rev. Lett.* **92** 115507 (2004)
236. Cleveland C L, Luedtke W D, Landman U *Phys. Rev. Lett.* **81** 2036 (1998)
237. Chushak Y G, Bartell L S *J. Phys. Chem. B* **105** 11605 (2001)
238. Nam H-S et al. *Phys. Rev. Lett.* **89** 275502 (2002)
239. Wales D J et al. *Adv. Chem. Phys.* **115** 1 (2000)
240. Wales D J *Energy Landscapes* (Cambridge: Cambridge Univ. Press, 2003)
241. Corti C W, Holliday R J, Thompson D T *Appl. Catal. A* **291** 253 (2005)
242. Hurst G S, Nayfeh M H, Young J P *Phys. Rev. A* **15** 2283 (1977)
243. Figger H et al. *Opt. Commun.* **33** 37 (1980)
244. Ochkin V N et al. *Sov. Phys. Usp.* **29** 260 (1986); *Usp. Fiz. Nauk* **148** 473 (1986)
245. Ochkin V N *Spektroskopiya Nizkotemperaturnoi Plazmy* (Spectroscopy of Low Temperature Plasma) (Moscow: Fizmatlit, 2006)
246. Ochkin V N *Spectroscopy of Low Temperature Plasma* (Weinheim: Wiley, 2009)
247. Göpel W *Sensors Actuators B* **4** 7 (1991)
248. Göpel W *Phil. Trans. R. Soc. A* **353** 333 (1995)
249. ISI Web of Knowledge. Web of Science, http://apps.isiknowledge.com/
250. Wolkenstein T *Electronic Processes on Semiconductor Surfaces During Chemisorption* (New York: Consultants Bureau, 1991); Translated from Russian: *Elektronnye Protsessy na Poverkhnosti Poluprovodnikov pri Khemosorbtsii* (Moscow: Nauka, 1987)
251. Madou M J, Morrison S R *Chemical Sensing with Solid State Devices* (London: Academic Press, 1991)
252. Ozin G A, Arsenault A C *Nanochemistry. A Chemical Approach to Nanomaterials* (Cambridge: RSC Publ., 2005)
253. Sergeev G B *Nanochemistry* (Amsterdam: Elsevier, 2006)
254. Gründler P *Chemical Sensors. An Introduction for Scientists and Engineers* (Berlin: Springer, 2007)
255. Bochenkov V E, Sergeev G B, in *Metal Oxide Nanostructures and Their Applications* Vol. 3 (Eds A Umar, Y-B Hahn) (Valencia, CA: American Sci. Publ., 2010) p. 31
256. Franke M E, Koplin T J, Simon U *Small* **2** 36 (2006)
257. Wang Ch et al. *Sensors* **10** 2088 (2010)
258. Jing Z, Zhan J *Adv. Mater.* **20** 4547 (2008)
259. Rout C S et al. *Solid State Commun.* **138** 136 (2006)
260. Di Francia G, Alfano B, La Ferrara V *J. Sensors* **2009** 659275 (2009)
261. Liu X et al. *Sensors* **12** 9635 (2012)
262. Konyukhov V Yu *Khromatografiya* (Chromatography) (Moscow: Lan, 2012)
263. Vargaftik N B *Tables on the Thermophysical Properties of Liquids and Gases* (Washington: Hemisphere Publ. Corp., 1975); Translated from Russian: *Spravochnik po Teplofizicheskim Svoistvam Gazov i Zhidkostei* (Moscow: Energoatomizdat, 1972)
264. Chahabra A, Herrmann H J, Landau D P, in *Fractals in Physics. Proc. of the Sixth Trieste Intern. Symp. on Fractals in Physics, ICTP, Trieste, Italy, July 9–12, 1985* (Eds L Pietronero, E Tosatti) (Amsterdam: North-Holland, 1986) p. 179
265. Laroussi M, Lu X *Appl. Phys. Lett.* **87** 113902 (2005)
266. Shin D H, Hong Y C, Uhm H S *IEEE Trans. Plasma Sci.* **34** 2464 (2006)
267. Smirnov B M, Tereshonok D V *Europhys. Lett.* **105** 35001 (2014)
268. Kim K-H *Atmos. Environ.* **39** 2235 (2005)